

Structural Characterization, Spectroscopic Profile, Molecular Docking, ADMET Properties, Molecular Dynamics Simulation Studies, and Molecular Mechanics Generalized Born Surface Area Analysis of 5-(Adamantan-1-yl)-4-butyl-2,4-dihydro-3H-1,2,4-triazole-3-thione as a Potential COX Inhibitor

Lamya H. Al-Wahaibi, Ali A. El-Emam,* Mohammed S. M. Abdelbaky, Santiago Garcia-Granda, Anushree Maurya, Mamta Pal, Zohra Siddiqui, Raj Shukla, Shilendra K. Pathak, Ruchi Srivastava, Vikas K. Shukla, Onkar Prasad, and Leena Sinha*



Cite This: *ACS Omega* 2024, 9, 26651–26672



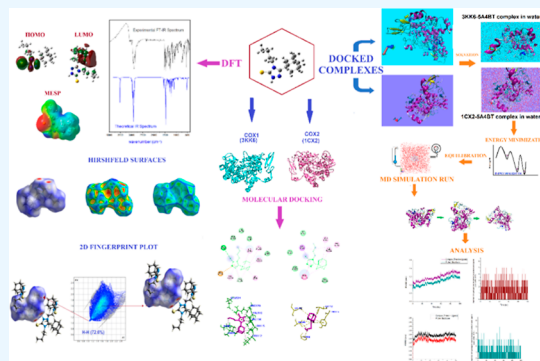
Read Online

ACCESS |

Metrics & More

Article Recommendations

ABSTRACT: Employing a synergistic combination of theoretical density functional theory (DFT) and experimental techniques, we conducted a comprehensive analysis elucidating the structural and pharmacological attributes of 5-(adamantan-1-yl)-4-butyl-2,4-dihydro-3H-1,2,4-triazole-3-thione (SA4BT) as a potent COX inhibitor. The X-ray crystallographic data of SA4BT showed the pivotal role played by weak interactions, notably π - π and C-H- π interactions, alongside hydrogen bonding, in orchestrating the intricate supramolecular architectures within the crystalline lattice. A quantitative analysis of the arrangement of the crystal structure, as well as both inter- and intramolecular interactions, was conducted using Hirshfeld surfaces and 2D fingerprint plots. Additionally, a comprehensive examination of the IR spectra was undertaken, employing both experimental methods and theoretical DFT techniques, to elucidate the vibrational characteristics of the compound. The strength of intermolecular N-H...S hydrogen bonding and charge transfer within the system was assessed through natural bonding orbital analysis. Moreover, Bader's atoms in molecules theory was employed to estimate the strength of intermolecular hydrogen bonds, revealing strong interactions within the SA4BT dimer. The title compound exhibited binding affinities of -6.4 and -6.5 kcal/mol for COX1 (PDB 3KK6) and COX2 (1CX2) target proteins, respectively. For the first time, predictions regarding ADMET properties, drug-likeness, and toxicity, including favorable bioavailability, along with 100 ns molecular dynamics simulations, binding free energy, and energy decomposition per residue in the binding cavity of the protein from molecular mechanics generalized born surface area approach, collectively indicate the potential of SA4BT as a nonselective COX inhibitor.



1. INTRODUCTION

Recognized for its hydrophobic traits, adamantane is a unique hydrocarbon that offers promise in enhancing the pharmacokinetic properties of a large number of drugs. By incorporating the adamantane moiety into molecules with suboptimal pharmacokinetics, the resulting derivatives often display improved drug-like characteristics, including superior absorption and an extended half-life.¹ The allure of the adamantane core has been long-standing in the realm of medicinal chemistry, especially since many of its modified derivatives showcase a diverse array of therapeutic potentials. The medical significance of adamantane-based compounds became particularly evident with the introduction of amantadine^{2,3} and rimantadine,⁴ which have proven effective against influenza A viral infections. Additionally, tromantadine was synthesized to

treat skin-related issues caused by the herpes simplex virus.⁵ The adamantane framework is not only integral to combatting viral infections but also underpins the pharmacodynamics of various modern anticancer drugs.^{6–10}

Derivatives of adamantane, well recognized for their anticancer,^{6–10} antiviral,^{11–13} and antibacterial properties,^{14–16} have also been a focal point of attention for their potential anti-inflammatory properties among medicinal chemists.^{17–24}

Received: April 11, 2024

Revised: May 22, 2024

Accepted: May 24, 2024

Published: June 5, 2024



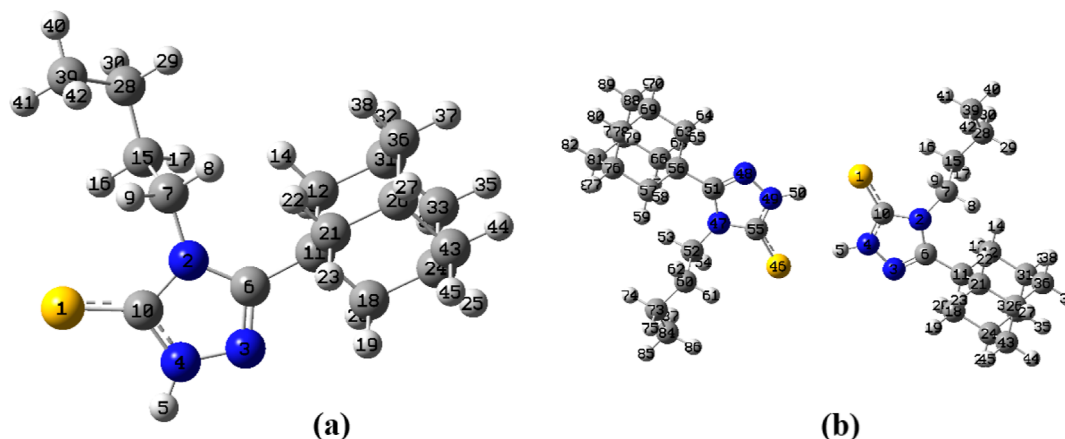


Figure 1. Optimized geometry of (a) 5A4BT and (b) its dimer at the DFT/B3LYP/6-311+G(d, p) level of theory.

Adamantane derivatives have been developed as anti-inflammatory agents consisting of two lipophilic center-linked oxime ethers, oxime esters, amides, and symmetric alcohol bridges.¹⁴ Several adamantane compounds of thiazolyl-*N*-substituted amides were synthesized and evaluated for their anti-inflammatory-, lipoxygenase-, and cyclooxygenase-inhibiting properties by Kouatly et al.¹⁷ The proposition that the substitution of an adamantyl ring for a phenyl ring could lead to opportunities in medicinal chemistry has been made by Fresno et al.,¹⁹ documenting the synthesis of adamantyl counterparts of paracetamol that exhibited significant analgesic properties.

It has also been observed that 1,2,4-triazole compounds and their *N*-mannich bases exhibit strong anti-inflammatory properties.^{14–17} Triazole heterocycles that incorporate sulfur through thione and mercapto substitution exhibit greater potency in comparison to their parent compounds.¹⁶ The induction of a thione moiety at the 3- or 5-position has been established, resulting in the augmentation of biological activity associated with the triazole group.¹⁶

In the pursuit of exploring the structural and pharmacological attributes of adamantane derivatives,^{14–18} this study provides an in-depth investigation of 5-(adamantan-1-yl)-4-butyl-2,4-dihydro-3*H*-1,2,4-triazole-3-thione (SA4BT), a hybrid compound incorporating both the adamantyl moiety and the triazole-thiol group. Synthesis of the thione tautomer of the title compound and its analgesic and anti-inflammatory activities have already been reported.¹⁴ We present a comprehensive study on the properties of the title compound using an amalgamation of theoretical computational and experimental methodologies, with the goal of uncovering the title compound's medical applications as a potential COX inhibitor due to the established analgesic and anti-inflammatory activities of its tautomer. Hirshfeld surfaces and 2D fingerprint plots (FP) were utilized to analyze and quantitate the arrangement of crystals and the interactions between molecules within the crystal structure. Furthermore, an exhaustive analysis of the IR spectrum of SA4BT was conducted, encompassing both experimental and theoretical approaches. To gain a deeper understanding of its molecular structure, vibrational spectrum, and frontier molecular orbitals (FMOs), we employed first-principles calculations using density functional theory (DFT). Nonlinear optical properties have been calculated, and molecular electrostatic potential surface (MESP) which demonstrates attributes associated with

the distributions of charges has been plotted using the tools of quantum chemistry. Natural bonding orbital (NBO) analysis has been performed between the monomers and dimer forms to see how charges move around in the system and how strong the *N*–*H*⋯hydrogen bonding is between the two monomeric units of the compound. The strength of the intermolecular hydrogen bond was also estimated using Bader's atoms in molecules (AIM) theory.²⁵ The dimer exhibiting *N*–*H*⋯*S* intermolecular hydrogen bonds has been analyzed to compute various topological parameters, such as electronic charge density and its Laplacian, kinetic and potential energy density, and bond ellipticity at bond critical points (BCPs) for a comprehensive analysis of the nature of the hydrogen bonding as well as the intermolecular hydrogen-bond strength. The compound's ADMET characteristics, toxicity, bioavailability, and suitability as a drug were evaluated to gauge its potential bioactivity. Additionally, the AutoDock Vina tool was employed for molecular docking studies to explore the potential of SA4BT as a COX inhibitor. To further assess its stability, a molecular dynamics (MD) simulation lasting 100 ns was performed for the protein–ligand complex, followed by free binding energy calculations using the molecular mechanics generalized born surface area (MM-GBSA) approach.²⁶

2. COMPUTATIONAL DETAILS

For computational purposes, the preliminary molecular 3D geometry of SA4BT stems directly from the experimental X-ray diffraction data. The gradient-corrected DFT²⁷ with Becke3 exchange²⁸ and Lee–Yang–Parr correlation functions (B3LYP)^{29,30} with 6-311+G(d, p) basis sets have been used in order to present an in-depth understanding on the structural characteristics of SA4BT. All the quantum chemical computations in this study have been performed using Gaussian 09 program package,³¹ while Gaussview 5.0 molecular visualization program³² was used for the analysis of the results. The calculations were conducted at the DFT-B3LYP/6-311+G(d, p) level to determine the vibrational wavenumbers using the harmonic approximation. The nonexistence of negative vibrational wavenumber validated the stability of the associated lowest energy configuration, located at the real minimum. The optimized molecular geometry of the investigated compound and its dimer are respectively shown in Figure 1a,b, whereas parameters associated with the optimized geometry at DFT/B3LYP with the 6-311+G(d, p) basis set along with the corresponding

Table 1. Computed Optimized Geometrical Parameters of 5A4BT at the B3LYP/6-311+G(d,p) Level along with Experimental Values

bond length	theo. (Å)	exp. (Å)	bond angle	theo. (°)	exp. (°)	dihedrals	theo. (°)	exp. (°)
S1–C10	1.67	1.69	C21–C26–H27	108.7	109.4	C18–C11–C21–H22	–179.2	–179.5
N2–C6	1.40	1.39	C21–C26–C36	109.6	110.4	C18–C11–C21–H23	–61.9	–61.0
N2–C7	1.47	1.47	C21–C26–C43	109.5	108.8	C18–C11–C21–C26	59.3	59.7
N2–C10	1.39	1.37	H27–C26–C36	109.7	109.4	C11–C12–C31–H32	–179.2	–179.6
N3–N4	1.36	1.37	H27–C26–C43	109.8	109.4	C11–C12–C31–C33	60.7	60.3
N3–C6	1.30	1.31	C36–C26–C43	109.5	109.3	C11–C12–C31–C36	–59.6	–59.7
N4–H5	1.01	0.86	C15–C28–H29	109.6	109.0	H13–C12–C31–H32	59.9	59.7
N4–C10	1.35	1.33	C15–C28–H30	107.9	109.0	H13–C12–C31–C33	–60.1	–60.4
C6–C11	1.52	1.51	C15–C28–C39	114.7	112.9	H13–C12–C31–C36	179.6	179.6
C7–H8	1.09	0.97	H29–C28–H30	105.8	107.7	H14–C12–C31–H32	–57.1	–58.9
C7–H9	1.09	0.97	H29–C28–C39	109.6	109.0	H14–C12–C31–C33	–177.2	–179.0
C7–C15	1.53	1.52	H30–C28–C39	108.9	109.0	H14–C12–C31–C36	62.5	61.0
C11–C12	1.55	1.54	C12–C31–H32	108.7	109.4	C7–C15–C28–H29	57.3	36.3
C11–C18	1.55	1.54	C12–C31–C33	109.7	109.9	C7–C15–C28–H30	172.0	153.7
C11–C21	1.56	1.54	C12–C31–C36	109.4	109.8	C7–C15–C28–C39	–66.4	–84.9
C12–H13	1.10	0.97	H32–C31–C33	109.8	109.4	H16–C15–C28–H29	178.5	157.2
C12–H14	1.09	0.97	H32–C31–C36	109.6	109.3	H16–C15–C28–H30	–66.7	–85.4
C12–C31	1.54	1.54	C33–C31–C36	109.6	109.1	H16–C15–C28–C39	54.8	35.9
C15–H16	1.09	0.97	C24–C33–C31	109.1	109.1	H17–C15–C28–H29	–64.3	–84.5
C15–H17	1.09	0.97	C24–C33–H34	110.2	109.9	H17–C15–C28–H30	50.4	32.9
C15–C28	1.54	1.53	C24–C33–H35	110.3	109.9	H17–C15–C28–C39	172.0	154.2
C18–H19	1.09	0.97	C31–C33–H34	110.1	109.8	C11–C18–C24–H25	179.9	179.5
C18–H20	1.09	0.97	C31–C33–H35	110.2	109.8	C11–C18–C24–C33	–60.2	–60.9
C18–C24	1.54	1.54	H34–C33–H35	107.0	108.3	C11–C18–C24–C43	60.2	59.7
C21–H22	1.09	0.97	C26–C36–C31	109.6	109.4	H19–C18–C24–H25	58.5	58.7
C21–H23	1.10	0.97	C26–C36–H37	110.0	109.8	H19–C18–C24–C33	178.4	178.3
C21–C26	1.54	1.54	C26–C36–H38	110.2	109.8	H19–C18–C24–C43	–61.2	–61.1
C24–H25	1.10	0.98	C31–C36–H37	110.0	109.8	H20–C18–C24–H25	–58.8	–59.7
C24–C33	1.54	1.52	C31–C36–H38	110.2	109.8	H20–C18–C24–C33	61.1	59.9
C24–C43	1.54	1.52	H37–C36–H38	106.8	108.2	H20–C18–C24–C43	–178.5	–179.5
C26–H27	1.10	0.98	C28–C39–H40	110.8	109.4	C11–C21–C26–H27	179.2	179.0
C26–C36	1.54	1.53	C28–C39–H41	111.0	109.4	C11–C21–C26–C36	59.3	58.6
C26–C43	1.54	1.53	C28–C39–H42	112.3	109.5	C11–C21–C26–C43	–60.9	–61.4
C28–H29	1.10	0.97	H40–C39–H41	107.9	109.5	H22–C21–C26–H27	56.8	58.3
C28–H30	1.10	0.97	H40–C39–H42	107.3	109.5	H22–C21–C26–C36	–63.0	–62.2
C28–C39	1.53	1.52	H41–C39–H42	107.4	109.5	H22–C21–C26–C43	176.8	177.8
C31–H32	1.10	0.98	C24–C43–C26	109.2	109.3	H23–C21–C26–H27	–60.4	–60.2
C31–C33	1.54	1.53	C24–C43–H44	110.2	109.8	H23–C21–C26–C36	179.7	179.3
C31–C36	1.54	1.53	C24–C43–H45	110.2	109.9	H23–C21–C26–C43	59.6	59.3
C33–H34	1.10	0.97	C26–C43–H44	110.1	109.8	C18–C24–C33–C31	59.7	60.1
C33–H35	1.10	0.97	C26–C43–H45	110.2	109.8	C18–C24–C33–H34	–61.3	–60.4
C36–H37	1.10	0.97	H44–C43–H45	106.9	108.3	C18–C24–C33–H35	–179.2	–179.4
C36–H38	1.10	0.97	dihedrals	theo. (°)	exp. (°)	H25–C24–C33–C31	178.9	179.7
C39–H40	1.09	0.96	C7–N2–C6–N3	–177.7	178.1	H25–C24–C33–H34	57.9	59.2
C39–H41	1.09	0.96	C7–N2–C6–C11	5.8	–1.3	H25–C24–C33–H35	–59.9	–59.8
C39–H42	1.09	0.96	C10–N2–C6–N3	0.5	0.1	C43–C24–C33–C31	–60.7	–60.3
C43–H44	1.10	0.97	C10–N2–C6–C11	–175.9	–179.4	C43–C24–C33–H34	178.3	179.3
C43–H45	1.10	0.97	C6–N2–C7–H8	–25.7	–16.3	C43–C24–C33–H35	60.4	60.2
bond angle	theo. (°)	exp. (°)	C6–N2–C7–H9	–141.5	–133.5	C18–C24–C43–C26	–59.8	–60.1
C6–N2–C7	130.6	131.5	C6–N2–C7–C15	97.6	105.1	C18–C24–C43–H44	179.1	179.4
C6–N2–C10	108.2	107.5	C10–N2–C7–H8	156.2	161.6	C18–C24–C43–H45	61.3	60.4
C7–N2–C10	121.2	121.0	C10–N2–C7–H9	40.4	44.4	H25–C24–C43–C26	–179.0	–179.9
N4–N3–C6	105.0	104.7	C10–N2–C7–C15	–80.4	–77.0	H25–C24–C43–H44	60.0	59.6
N3–N4–H5	120.9	123.4	C6–N2–C10–S1	178.3	179.8	H25–C24–C43–H45	–57.8	–59.4
N3–N4–C10	114.1	113.3	C6–N2–C10–N4	–0.8	0.1	C33–C24–C43–C26	60.7	60.0
H5–N4–C10	125.0	123.3	C7–N2–C10–S1	–3.2	1.5	C33–C24–C43–H44	–60.4	–60.5
N2–C6–N3	110.2	110.1	C7–N2–C10–N4	177.6	–178.2	C33–C24–C43–H45	–178.2	–179.4
N2–C6–C11	127.9	127.6	C6–N3–N4–H5	–179.2	–179.8	C21–C26–C36–C31	–60.6	–59.4
N3–C6–C11	121.9	122.3	C6–N3–N4–C10	–0.6	0.2	C21–C26–C36–H37	178.3	180.0
N2–C7–H8	108.3	108.9	N4–N3–C6–N2	0.0	–0.2	C21–C26–C36–H38	60.8	61.1

Table 1. continued

bond length	theo. (Å)	exp. (Å)	bond angle	theo. (°)	exp. (°)	dihedrals	theo. (°)	exp. (°)
N2–C7–H9	105.9	108.9	N4–N3–C6–C11	176.7	179.3	H27–C26–C36–C31	–179.9	–179.9
N2–C7–C15	112.9	113.4	N3–N4–C10–S1	–178.3	–179.9	H27–C26–C36–H37	59.0	59.5
H8–C7–H9	108.1	107.8	N3–N4–C10–N2	0.9	–0.2	H27–C26–C36–H38	–58.5	–59.3
H8–C7–C15	111.1	108.9	H5–N4–C10–S1	0.3	0.1	C43–C26–C36–C31	59.5	60.3
H9–C7–C15	110.4	108.9	H5–N4–C10–N2	179.5	179.8	C43–C26–C36–H37	–61.5	–60.3
S1–C10–N2	129.4	127.2	N2–C6–C11–C12	–56.5	–57.8	C43–C26–C36–H38	–179.0	–179.1
S1–C10–N4	128.0	128.5	N2–C6–C11–C18	–176.0	–176.1	C21–C26–C43–C24	60.2	60.8
N2–C10–N4	102.6	104.4	N2–C6–C11–C21	66.0	65.3	C21–C26–C43–H44	–178.6	–178.6
C6–C11–C12	112.7	111.4	N3–C6–C11–C12	127.4	122.9	C21–C26–C43–H45	–60.9	–59.7
C6–C11–C18	108.8	107.9	N3–C6–C11–C18	7.9	4.6	H27–C26–C43–C24	179.6	–179.6
C6–C11–C21	110.3	112.0	N3–C6–C11–C21	–110.1	–114.0	H27–C26–C43–H44	–59.3	–59.1
C12–C11–C18	107.8	107.9	N2–C7–C15–H16	60.9	42.5	H27–C26–C43–H45	58.4	59.8
C12–C11–C21	109.3	109.6	N2–C7–C15–H17	–55.2	–75.8	C36–C26–C43–C24	–59.9	–59.8
C18–C11–C21	107.7	107.9	N2–C7–C15–C28	–176.9	163.3	C36–C26–C43–H44	61.2	60.7
C11–C12–H13	109.3	109.6	H8–C7–C15–H16	–177.2	163.9	C36–C26–C43–H45	178.9	179.6
C11–C12–H14	111.0	109.7	H8–C7–C15–H17	66.7	45.5	C15–C28–C39–H40	–175.6	–180.0
C11–C12–C31	110.3	110.1	H8–C7–C15–C28	–55.1	–75.3	C15–C28–C39–H41	–55.8	–60.0
H13–C12–H14	107.0	108.2	H9–C7–C15–H16	–57.3	–78.9	C15–C28–C39–H42	64.5	60.0
H13–C12–C31	110.2	109.6	H9–C7–C15–H17	–173.4	162.8	H29–C28–C39–H40	60.7	58.7
H14–C12–C31	108.9	109.7	H9–C7–C15–C28	64.8	42.0	H29–C28–C39–H41	–179.4	178.7
C7–C15–H16	108.4	109.5	C6–C11–C12–H13	–57.8	–56.6	H29–C28–C39–H42	–59.2	–61.3
C7–C15–H17	109.0	109.5	C6–C11–C12–H14	60.0	62.0	H30–C28–C39–H40	–54.6	–58.7
C7–C15–C28	113.1	110.8	C6–C11–C12–C31	–179.1	–177.3	H30–C28–C39–H41	65.2	61.3
H16–C15–H17	107.0	108.1	C18–C11–C12–H13	62.3	61.7	H30–C28–C39–H42	–174.5	–178.7
H16–C15–C28	109.9	109.4	C18–C11–C12–H14	–179.9	–179.7	C12–C31–C33–C24	–60.1	–60.2
H17–C15–C28	109.3	109.4	C18–C11–C12–C31	–59.0	–59.0	C12–C31–C33–H34	61.0	60.3
C11–C18–H19	109.5	109.5	C21–C11–C12–H13	179.1	178.9	C12–C31–C33–H35	178.7	179.3
C11–C18–H20	109.4	109.5	C21–C11–C12–H14	–63.1	–62.5	H32–C31–C33–C24	–179.4	179.7
C11–C18–C24	110.7	110.6	C21–C11–C12–C31	57.8	58.2	H32–C31–C33–H34	–58.4	–59.8
H19–C18–H20	106.4	108.1	C6–C11–C18–H19	–56.8	–59.1	H32–C31–C33–H35	59.4	59.2
H19–C18–C24	110.3	109.5	C6–C11–C18–H20	59.6	59.3	C36–C31–C33–C24	60.1	60.2
H20–C18–C24	110.3	109.5	C6–C11–C18–C24	–178.6	–179.9	C36–C31–C33–H34	–178.8	–179.3
C11–C21–H22	110.9	109.6	C12–C11–C18–H19	–179.3	–179.6	C36–C31–C33–H35	–61.1	–60.3
C11–C21–H23	109.0	109.6	C12–C11–C18–H20	–62.9	–61.2	C12–C31–C36–C26	60.7	60.0
C11–C21–C26	110.3	110.3	C12–C11–C18–C24	58.9	59.6	C12–C31–C36–H37	–178.3	–179.5
H22–C21–H23	106.8	108.1	C21–C11–C18–H19	62.8	62.1	C12–C31–C36–H38	–60.8	–60.6
H22–C21–C26	109.5	109.6	C21–C11–C18–H20	179.2	–179.5	H32–C31–C36–C26	179.7	179.9
H23–C21–C26	110.3	109.6	C21–C11–C18–C24	–59.0	–58.7	H32–C31–C36–H37	–59.2	–59.5
C18–C24–H25	108.6	109.3	C6–C11–C21–H22	–60.6	–60.9	H32–C31–C36–H38	58.3	59.3
C18–C24–C33	109.8	109.2	C6–C11–C21–H23	56.7	57.6	C33–C31–C36–C26	–59.7	–60.5
C18–C24–C43	109.7	109.6	C6–C11–C21–C26	177.9	178.4	C33–C31–C36–H37	61.4	60.1
H25–C24–C33	109.7	109.3	C12–C11–C21–H22	63.9	63.3	C33–C31–C36–H38	178.9	178.9
H25–C24–C43	109.6	109.3	C12–C11–C21–H23	–178.8	–178.2			
C33–C24–C43	109.5	110.0	C12–C11–C21–C26	–57.6	–57.5			

experimental (XRD) values are reported in Table 1. In order to determine the strength of the hydrogen bonds that exist between monomeric units, the theory of AIM developed by Bader²⁴ has been used. The harmonic vibrational wavenumbers that were computed have been scaled by 0.983 for wavenumbers up to 1700 cm^{–1} and by 0.958 for wavenumbers higher than 1700 cm^{–1}.³³ This was done in order to eliminate the systematic foibles that were brought about by the incompleteness of the basis set and vibrational anharmonicity.³⁴ In consonance with Pulay et al.³⁵ and Fogarasi et al.,³⁶ the normal coordinate analysis of 5A4BT has been done after constructing a nonredundant set of 129 (i.e., 3*n* – 6) local symmetry coordinates using the complete set of standard internal coordinates. The allocations of the computationally determined normal vibrational modes were determined using

the MOLVIB software (version V7.0-G77) developed by Sundius^{37–39} in tandem with the corresponding potential energy distributions (PEDs). The infrared spectrum was simulated employing a pure Lorentzian band shape with a full width at half-maximum (FWHM) of 5 cm^{–1}. FMOs such as HOMO, LUMO, and their energy gap have been analyzed.

We used the DFT/B3LYP-6-311+G(d, p) level of theory to figure out the nonlinear optical properties of 5A4BT and its electric moments. Based on Buckingham's definitions,⁴⁰ the α , y , and z components of the electric moments were utilized to find the total dipole moment, the average polarizability, and the total first static hyperpolarizability. The α and β_{tot} values, as obtained from the Gaussian output file, were in atomic units (au), so eventually they were changed to electrostatic units

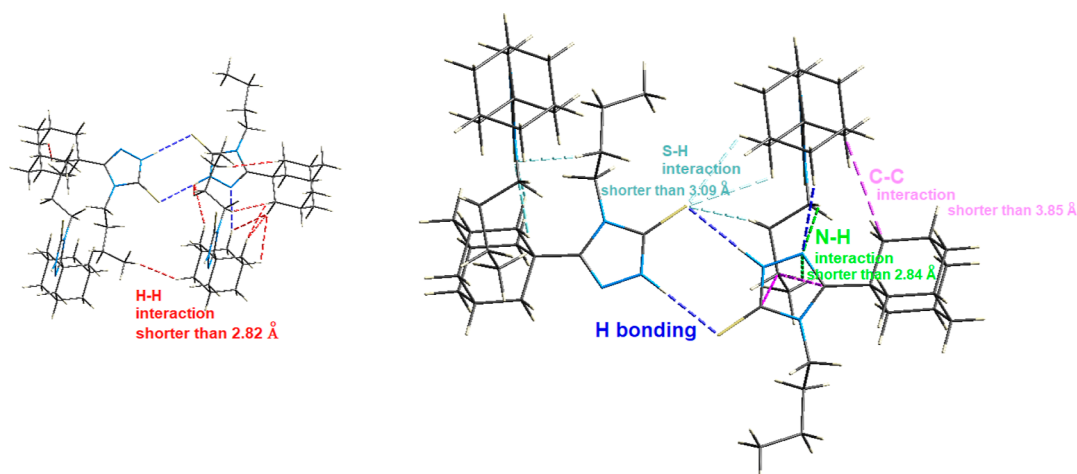


Figure 2. X-ray crystal structure of 5A4BT.

(esu) (α ; 1 au = 0.1482×10^{-24} esu, β ; 1 au = 8.6393×10^{-33} esu).

We conducted natural bond orbital (NBO)⁴¹ computations for both monomer and dimer structures to analyze the transfer of electron density and the resulting stabilization. Intermolecular as well as intramolecular interactions between bonding and antibonding orbitals affect the occupancy of the ideal Lewis structure. The stabilization energy for every d (donor) \rightarrow a (acceptor) delocalization was determined using the formula

$$E_{da}^{(2)} = q_d \frac{\hat{I}(d, a)^2}{\Delta\epsilon}$$

with $\Delta\epsilon$ calculated as $\epsilon_a - \epsilon_d$; here, ϵ_a and ϵ_d are the diagonal elements, and $\hat{I}(d, a)$ are the off diagonal elements of the NBO matrix, while q_d corresponds to donor orbital occupancy.

In addition to this, Bader's theory of AIM²⁴ has been employed for the estimation of the strength of hydrogen bonds that exist between molecules. In addition to the AIM analysis, the noncovalent interaction (NCI) technique was used to gain insights into the interactions between the two 5A4BT monomers. This analysis relied on electron density $\rho(r)$ and reduced density gradient (RDG) functions to reveal weak interaction regions.⁴² The RDG equation is as follows

$$\text{RDG} = \frac{1}{2(3\pi^2)^{1/3}} \frac{|\nabla\rho(r)|}{\rho(r)^{4/3}}$$

This approach highlights regions with small $\rho(r)$, effectively isolating weak interaction regions and allowing us to differentiate interaction types by using color-coding. Specifically, blue represents $\rho > 0$ and $\lambda_2 < 0$, green signifies $\rho \sim 0$ and $\lambda_2 \sim 0$, while red indicates $\rho > 0$ and $\lambda_2 > 0$ on the RDG isosurface. This method not only identifies weak interaction regions but also characterizes the nature of these interactions based on color-coded indicators.

5A4BT was subjected to docking simulations within the appropriate binding cavity of both COX-1 (PDB: 3KK6 in complex with celecoxib) and COX-2 (PDB: 1CX2 cocrystallized with SC-558) using the Auto Dock Vina software.⁴³ Auto Dock Vina is a widely recognized open-source docking tool that is known for its speed and popularity. Vina employs a straightforward scoring function and efficient gradient-

optimization conformational search, making it a versatile and efficient choice for such simulations.

Most biomolecular systems exhibit dynamic behavior, which means that their conformations change over time. On the other hand, the molecular models that are recorded in files structured as PDB are static. To have an insight on the dynamic behavior of 5A4BT in complex with the target proteins, MD simulation has been carried out using GROMACS MD program (2021.1version).^{44–48} The MD simulations on the docked protein–ligand complex have been performed, and results are analyzed.

3. RESULTS AND DISCUSSION

3.1. Molecular Geometry. The title compound and its dimer (Figure 1) were optimized at the DFT-B3LYP/6-311+G(d, p) level of theory. The ground-state energy of the title molecule, as determined by calculations, is found to be -32312.56 eV. The dihedral angles of the 1,2,4-triazole ring moiety in the molecule have values close to 0 or 180°, indicating a planar conformation for this moiety. The lengths of the N–N bond in the triazole ring and the connected C–S bond were calculated to be 1.36 and 1.67 Å, respectively. The bond length between C7 and N2 (1.47 Å) that connects the ring with the butyl group is comparatively longer than the other carbon–nitrogen bond lengths of the ring, which fall within the range of 1.30–1.40 Å. The bond length between the C10 and N2 atoms (1.388 Å) is somewhat shorter than the bond length between the C6 and N2 atoms (1.396 Å) in the ring, perhaps due to the presence of a sulfur (S) atom linked to the C10 atom. The carbon–carbon bond lengths of the butyl group exhibit a close approximation of 1.53 Å. The dihedral angles obtained for the orientation of the 1,2,4-triazole ring relative to the adamantane ring are as follows: N2–C6–C11–C12 = 56.50° and N3–C6–C11–C18 = 7.90°. The adamantyl group is composed of three fused cyclohexane rings that are placed in the “armchair” conformation. The average carbon–carbon bond length of the adamantyl cage is measured to be around 1.54 Å, a value that closely resembles the bond length seen in diamond. The bond length between carbon atoms C6 and C11, which links the triazole ring with the adamantyl cage, is 1.52 Å. This length is the shortest among all the carbon–carbon bond lengths present in the molecule.

The ideal angle for the carbon chain in adamantane is 109° as all of the carbon atoms are in the sp^3 hybridization state.

Table 1 compares both experimental and calculated bond lengths, bond angles, and dihedral angles of 5A4BT that define the structural features. The calculated geometric parameters of 5A4BT are close to the respective experimental values, and thus the optimized structure can be used to compute other useful parameters, such as vibrational frequencies, electronic properties, and electric moments. The trivial differences between some theoretical and experimental values can be due to the presence of intermolecular hydrogen bonding present in the crystal structure.

3.2. HS Analysis and Supramolecular Attributes. The X-ray crystal structure of the title compound indicates that hydrogen bonding combines with other weaker forces such as $\pi\cdots\pi$ and C–H $\cdots\pi$ interactions maintains the supramolecular framework (Figure 2). Molecular interactions, even weaker ones, have a significant impact on material characteristics and on physical, chemical, as well as biological processes.

The HS technique is regarded as a simple tool for ascertaining interactions between molecules. The interactions between the atoms and molecules within the crystal determine the form of the HS. In a crystal, the HS is identified as the area surrounding a molecule for which the molecular weight function is $w(r) \geq 1/2$. This function is expressed as the ratio of the spherically averaged atomic electron density ($\rho_{\text{promolecule}}$) of a sum of spherical atoms for the molecule (the promolecule) and the sum over the crystal (the procrystal), or $\rho_{\text{procrystal}}$. Specifically, it is the region where the promolecule's electron density contribution to the procrystal outweighs that of all other molecules present in the crystal.

Figure 3a,b respectively depicts the Hirshfeld surfaces of 5A4BT and its dimer mapped over d_{norm} , while Figure 3c,d

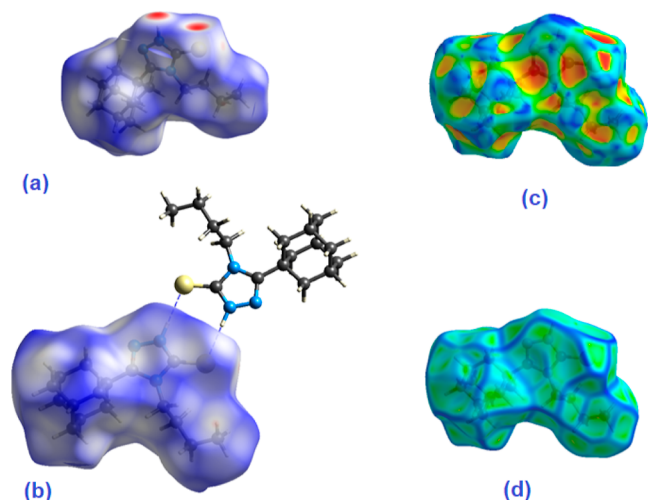


Figure 3. Hirshfeld surfaces mapped over d_{norm} for (a) 5A4BT and (b) dimer of 5A4BT. Hirshfeld surfaces of 5A4BT mapped over (c) shape index and (d) curvedness.

shows the Hirshfeld surfaces of 5A4BT mapped over the shape index and curvedness, respectively. On the d_{norm} surface, red is used to highlight intermolecular contacts where the distance is less than the sum of their van der Waals radii. Conversely, interactions nearly at a distance equal to the sum of van der Waals radii are depicted white, while longer contacts are depicted blue. Two big dark red spots on the surface are due to N–H \cdots S hydrogen bonding. The smaller light red spot near the methyl group shows H \cdots H interaction.

Utilizing the shape index and curvedness surfaces, the planar stacking ($\pi\cdots\pi$) interaction within the crystal can be identified. The shape index of the HS is indicated by the presence of close red and blue triangles. The presence/absence of such triangles indicates the presence/absence of $\pi\cdots\pi$ interactions. Figure 3c unequivocally illustrates the presence of $\pi\cdots\pi$ interactions within the compound under consideration. Flat green sections divided by blue borders are seen in the mapping of the curvedness on the HS. The $\pi\cdots\pi$ and ring stacking interactions are the clearly apparent flat sections on the curvedness surface. Quantitative parameters such as volume, area, globularity, and asphericity have been calculated using HS and found to be 379.05 Å³, 321.34 Å², 0.788, and 0.138, respectively.

The 2D FPs (Figure 4), which are achieved from the HS, offer a graphical representation of the occurrence of every combination of de and di across the molecule's surface. As a result, they reveal not only the presence of intermolecular interactions but also the relative surface area associated with each type of interaction. Wing-like peripheral spikes shown in the FP account for S–H/H–S contact, constituting 12.4% of the HS. H–H interactions account for the majority of the center region (72.6%). The interaction N–H/H–N accounts for 10.1% of the HS.

Using NBO (natural bond orbital)⁴¹ analysis, AIM theory,²⁴ and NCI (noncovalent interactions) method, the strength of intra-/intermolecular interactions of 5A4BT has been explored. In addition to N–H \cdots S hydrogen bonding between the monomeric units, the presence of a variety of wide bands in the 2900–3100 cm^{−1} region in the FT-IR spectrum involving CH₂ and CH₃ stretching vibrations indicates a chemical system with an extensive system of H \cdots H interactions. The FPs (Figure 4) also show the dominance of H \cdots H interactions.

The NBO analysis makes use of the second-order Fock matrix to assess the donor–acceptor interactions.⁴⁹ It gives information about lone pairs, chemical bonds, and the general distribution of electrons within molecules. The value of stabilization energy E(2) decides the strength of interaction, and its magnitude is higher for the strong interaction between the electron donor and electron acceptor. NBO analysis proves invaluable in elucidating electron resonance and delocalization, offering insights into reactivity and molecular properties' prediction.^{50,51} The NBO analysis of 5A4BT is performed using the Gaussian 09 program, and important interactions are shown in Table 2.

The lone pair LP (2) of S1 interacts with antibonding σ^* (N2–C10), and this interaction results in the stabilization of 13.78 kcal/mol of energy. The lone pair LP (1) of N4 interacts with antibonding σ^* (S1–C10) with the highest stabilization energy of 74.12 kcal/mol, and the interaction between the lone pair of N2 LP(1) and σ^* (S1–C10) gives the second highest E(2) energy of 66.78 kcal/mol. An interesting and strong interaction between the lone pair of N2 LP (1) and the antibonding π^* (N3–C6) is calculated with the stabilization energy of 44.46 kcal/mol. The interaction between the lone pair LP (1) of N4 and π^* (N3–C6) gives an E(2) energy of 24.66 kcal/mol. To evaluate intermolecular hydrogen bonding in the 5A4BT dimer, NBO analysis was performed on the dimer. Charge transfer from the sulfur (S1) (LP2) lone pair to σ^* (N49–H50) yields 0.07004e occupancy, whereas charge transfer from S46 (LP2) to σ^* (N4–H5) yields 0.07001e occupancy. A considerable interaction energy of 16.24 kcal/mol was found for the hydrogen bonds (N49–H50 \cdots S1 and

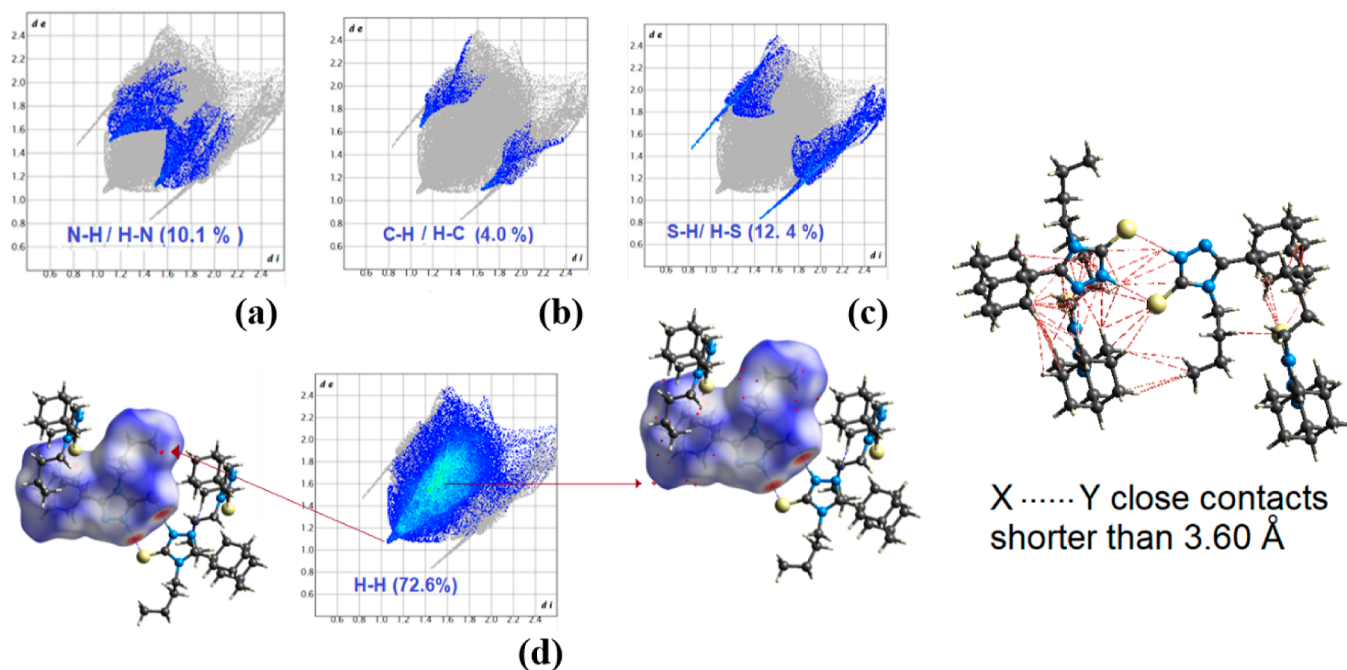


Figure 4. Two-dimensional FPs of 5A4BT depicting contributions from (a) N–H/H–N, (b) C–H/H–C, (c) S–H/H–S, and (d) H–H interactions.

Table 2. Second-Order Perturbation Theory Analysis of the Fock Matrix in the NBO Basis for B3LYP/6-311G++(d,p)

donor	type	ED/e (d) ^a	acceptor	type2	ED/e (a) ^a	$E_{da}(2)$ kcal/mol ^b	$\epsilon_d - \epsilon_a$ au ^c	$\hat{I}(d,a)$ au ^d
Monomer (Gas Phase)								
S1–C10	σ	1.99069	S1–C10	σ^*	0.58268	6.82	0.21	0.04
N2–C6	σ	1.9815	S1–C10	π^*	0.0012	4.39	1.11	0.062
N3–N4	σ	1.9815	C6–C11	σ^*	0.03598	4.95	1.26	0.071
C11–C18	σ	1.9624	N2–C6	σ^*	0.0477	5.56	0.99	0.067
S1	LP (1)	1.9849	C10	RY*(3)	0.00839	4.45	1.76	0.079
S1	LP (1)		N2–C10	σ^*	0.08046	4.09	1.08	0.06
S1	LP (2)	1.86039	N2–C10	σ^*	0.00004	13.78	0.58	0.081
S1	LP (2)	1.9849	N4–C10	σ^*	0.071	11.96	0.64	0.079
N2	LP (1)	1.5776	S1–C10	σ^*	0.58268	66.78	0.21	0.11
N2	LP (1)		N3–C6	π^*	0.297	44.46	0.27	0.102
N2	LP (1)		C7–C15	σ^*	0.01993	5.13	0.65	0.058
N3	LP (1)	1.9359	C6	RY*(1)	0.011	5.84	1.41	0.082
N3	LP (1)		N2–C6	σ^*	0.04777	6.2	0.83	0.064
N3	LP (1)		N4–C10	σ^*	0.071	7.42	0.87	0.072
N4	LP (1)	1.6003	S1–C10	σ^*	0.58268	74.12	0.22	0.118
N4	LP (1)		N3–C6	π^*	0.297	24.66	0.28	0.076
Dimer (Gas Phase)								
S1	LP (1)	1.97886	N49–H50	σ^*	0.07004	2.52	1.06	0.047
S1	LP (2)	1.83624	N49–H50	σ^*	0.07004	16.24	0.59	0.090
S46	LP (1)	1.97886	N4–H5	σ^*	0.07001	2.52	1.06	0.047
S46	LP (2)	1.83624	N4–H5	σ^*	0.07001	16.24	0.59	0.090

^aED: electron density. ^b $E_{da}(2)$: mean energy of hyperconjugative interactions. ^cEnergy difference between the donor and acceptor, d and a, NBOs. ^d $\hat{I}(d,a)$ is the Fock matrix element between the d and a NBOs.

N4–H5...S46), indicating significant hydrogen bonding in the 5A4BT monomeric units.

Bader's "atoms in molecules" (AIM) theory²⁴ has become a crucial tool for depicting the molecular topology. It provides topological parameters by determining the BCPs between two neighboring atoms. As a result, this is an appropriate method for analyzing the H-bonding and other interactions in a variety of molecular systems. Various topological parameters derived from AIM analysis, such as the charge density at BCPs

($\rho(\text{BCP})$), its Laplacian ($\nabla^2\rho(\text{BCP})$), kinetic energy density $G(r)$, and potential energy density $V(r)$ at the BCP of interacting atoms or fragments,^{52,53} have proven to be very effective in describing the existence and strength of hydrogen bonds. The topological analysis of the title molecule reveals the presence of three BCPs, two representing the equivalent intermolecular (N–H...S and S...H–N) hydrogen bonds while another one representing the intramolecular (C–S...H–C) H bond. For closed-shell interactions, such as those in ionic

bonds, hydrogen bonds, and van der Waals molecules, the value of $\rho(\text{BCP})$ should be low (0.002–0.040 au) and $\nabla^2\rho(\text{BCP})$ should be positive lying in the range 0.015–0.15 au, as per the criteria laid out by Koch and Popelier.⁵³ The strength of weak C–S...H–C interaction using AIM theory has been calculated to be 1.21 kcal/mol. The topological parameters for the observed intermolecular hydrogen bonds in the dimer of the title compound are given in Table 3.

Table 3. Topological Parameters for Hydrogen-Bonded Interactions in the SA4BT Molecule

parameters	S1...H50–N/N–HS...S46
electron density ($\rho(\text{BCP})$) au	0.02264
laplacian of electron density $\nabla^2\rho(\text{BCP})$ au	0.04640
bond ellipticity	0.06133
Lagrangian kinetic energy $G(r)$ au	0.01183
Hamiltonian kinetic energy $K(r)$ au	0.00023
potential energy density $V(r)$ au	–0.01207
eigen value λ_1	–0.02570
eigen value λ_2	–0.02421
eigen value λ_3	0.09631
$ V(r) /G(r)$ (au)	1.020
H-bond energy (kcal/mol)	3.79

According to Table 3, the charge density values at BCPs and its Laplacian ($\nabla^2\rho$ BCP) are greater than what is required for the formation of a hydrogen bond, suggesting strong H-bonded interactions between the SA4BT dimer. To determine the energy values of H bonds, Espinosa et al.⁵⁴ put forward the equation $E = V(r)_{\text{BCP}}/2$, which shows that increasing the potential energy density $V(r)$ at BCP leads to the strengthening of H bonds. The energy associated with (N–H...S) intermolecular interactions was determined to be 3.79 kcal/mol. The critical points found in the hydrogen bonds are associated with two negative Eigen values (λ_1 and λ_2) and one positive Eigen value (λ_3).

An extension of the AIM theory, the RDG analytical approach, allows for the visual representation of weak interaction regions. It helps us to distinguish between different interaction regions using the color-filled RDG isosurface. The 2D-RDG graph is presented in Figure 5. Blue spikes that showed up on the $\text{sign } \lambda_2(r)\rho(r)$ axis between –0.03 and –0.05 au indicated that hydrogen-bonded interactions exist in the system.

3.3. Electronic Moments. The dipole moment, expressed as a 3D vector, provides insights into the distribution of molecular charges. Therefore, it serves as a descriptor for illustrating how charges move within the molecule. Additionally, it plays a pivotal role in the study of nonbonded dipole–dipole interactions that occur between molecules. The elevated dipole moment value in the case of the title molecule (5.382 D) may primarily be attributable to a general imbalance in charge distribution, which is also obvious from the surface plot of the molecular electrostatic potential (MESP).

Polarizability, an essential characteristic, quantifies the susceptibility of an electron cloud to deformation under the influence of an electric field. Moreover, it has a direct effect on the binding affinity of a ligand. A ligand with high polarizability has a tendency to bind more firmly to its target compared to a ligand with low polarizability.⁵⁵ Many proteins have been shown to possess ligand-binding sites that exhibit a significant concentration of charged side chains. These side chains have

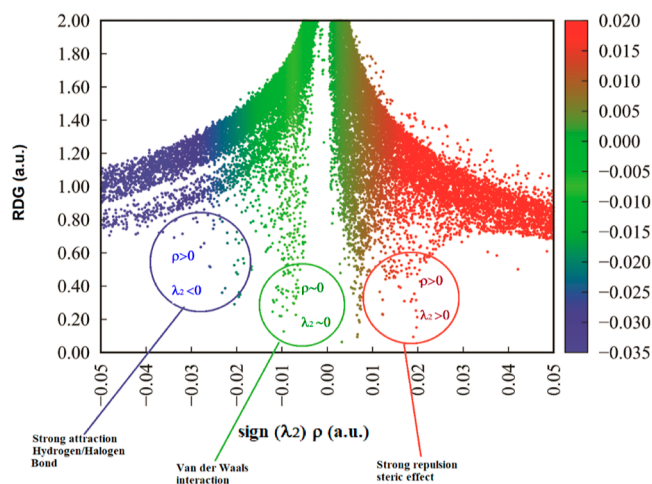


Figure 5. Scatter-graph of RDG vs $\text{sign}(\lambda_2)\rho$.

the ability to polarize tiny organic molecules and hence impact the binding process with the protein.⁵⁶ The title molecule's computed mean polarizability is 32.876×10^{-24} esu. Hyperpolarizability is linked to the movement of intra-molecular charge, which happens when the electronic cloud shifts inside the π -conjugated network from electron donors to acceptors. Therefore, this function functions as a criterion for evaluating both linear and nonlinear optical behaviors. The first static hyperpolarizability of the compound is calculated to be 2.152×10^{-30} esu. The components as well as the total magnitude of dipole moment, polarizability, and hyperpolarizability of SA4BT are collected in Table 4.

Table 4. Dipole Moment, Polarizability, and First Hyperpolarizability of SA4BT Molecule, Computed at the DFT-B3LYP/6-311+G(d, p) Level

Dipole moments (Debye)		First hyperpolarizability (au)	
μ_x	4.725	β_{xxx}	–79.687
μ_y	2.560	β_{xxy}	2.839
μ_z	–0.284	β_{xyy}	–81.707
μ_{total}	5.382	β_{yyy}	–58.770
Polarizability (au)		β_{xyz}	–4.028
α_{xx}	274.216	β_{yyz}	21.898
α_{xy}	6.563	β_{xzz}	–75.186
α_{yy}	217.370	β_{yzz}	–15.201
α_{xz}	–5.955	β_{zzz}	6.603
α_{yz}	2.71	β_{total} (au)	249.110
α_{zz}	173.92	β_{total} (esu)	2.152×10^{-30}
α_{mean} (au)	221.835		
α_{mean} (esu)	32.876×10^{-24}		

3.4. Vibrational Analysis. The molecule SA4BT consists of 45 atoms without exhibiting any symmetry and thus contains $3n - 6$ (129) normal vibrational modes in the functional and fingerprint areas. The FT-IR spectrum of the title compound was experimentally recorded and theoretically calculated using the harmonic approximation at the DFT/B3LYP/6-311+G(d, p) level of theory. As a result of the electron correlation effects and shortcomings in the basis set, the harmonic wavenumbers that are computed are often greater than the corresponding experimental values. It is possible to address these disparities by calculating anharmonic corrections manually, by injecting a scalar field, or even by

Table 5. Comparison of the Observed IR Wavenumbers (cm^{-1}) with Theoretical Harmonic Wavenumbers (cm^{-1}) and Infrared Intensities (I^{IR}) for 5A4BT^a

s. no.	theoretical (cm^{-1})		exp. (cm^{-1})	IR int.	PED {relative phases and % contribution (more than 5%)}
	unsc.	sc.			
1	3671	3517		105	$\nu(\text{N-H})(99)$
2	3129	2998	3092	13.4	$\nu_{\text{asym}}(\text{C7H}_2)(87)$
3	3094	2964	3058	45.2	$\nu_{\text{asym}2}(\text{CH}_3)(90)$
4	3089	2959	3006	34.7	$\nu_{\text{asym}1}(\text{CH}_3)(96)$
5	3084	2954	2930	34.0	$\nu_{\text{asym}}(\text{CH}_2)(\text{R}2)(83) + \nu_{\text{sym}}(\text{CH}_2)(\text{R}2)(12)$
6	3082	2953		38.7	$\nu_{\text{asym}}(\text{CH}_2)(\text{R}2)(88) + \nu_{\text{sym}}(\text{CH}_2)(\text{R}2)(10)$
7	3077	2948		16.0	$\nu_{\text{asym}}(\text{C15H}_2)(75) + \nu_{\text{sym}}(\text{C7H}_2)(20)$
8	3073	2944		12.5	$\nu_{\text{sym}}(\text{C7H}_2)(60) + \nu_{\text{asym}}(\text{C15H}_2)(15)$
9	3064	2935		24.4	$\nu_{\text{asym}}(\text{CH}_2)(\text{R}2)(92)$
10	3050	2922	2901	107.5	$\nu_{\text{asym}}(\text{CH}_2)(\text{R}2)(95)$
11	3047	2919		45.4	$\nu_{\text{sym}}(\text{CH}_2)(\text{R}2)(65) + \nu_{\text{asym}}(\text{CH}_2)(\text{R}2)(20)$
12	3046	2918		24.1	$\nu_{\text{asym}}(\text{C28H}_2)(46) + \nu_{\text{sym}}(\text{C15H}_2)(30)$
13	3044	2916		20.2	$\nu_{\text{asym}}(\text{CH}_2)(\text{R}2)(97)$
14	3043	2915		2.9	$\nu_{\text{asym}}(\text{CH}_2)(\text{R}2)(90)$
15	3037	2909		49.2	$\nu_{\text{sym}}(\text{CH}_2)(\text{R}2)(50) + \nu(\text{CH})(\text{R}2)(45)$
16	3033	2906		48.4	$\nu_{\text{sym}}(\text{C15H}_2)(35) + \nu(\text{CH})(\text{R}2)(25) + \nu_{\text{sym}}(\text{CH}_2)(\text{R}2)(20)$
17	3032	2905		65.9	$\nu(\text{CH})(\text{R}2)(35) + \nu_{\text{sym}}(\text{C15H}_2)(30) + \nu_{\text{sym}}(\text{CH}_2)(\text{R}2)(20) + \nu_{\text{asym}}(\text{C28H}_2)(15)$
18	3029	2902		78.6	$\nu(\text{CH})(\text{R}2)(65) + \nu_{\text{sym}}(\text{CH}_2)(\text{R}2)(34)$
19	3028	2901		37.0	$\nu_{\text{sym}}(\text{CH}_3)(95)$
20	3023	2896		34.0	$\nu(\text{CH})(\text{R}2)(37) + \nu_{\text{sym}}(\text{CH}_2)(\text{R}2)(34)$
21	3021	2894		5.5	$\nu_{\text{sym}}(\text{CH}_2)(\text{R}2)(60) + \nu(\text{CH})(\text{R}2)(34)$
22	3010	2884		17.1	$\nu_{\text{sym}}(\text{CH}_2)(\text{R}2)(60) + \nu(\text{CH})(\text{R}2)(30)$
23	3009	2883	2850	17.7	$\nu_{\text{sym}}(\text{CH}_2)(\text{R}2)(65) + \nu(\text{CH})(\text{R}2)(27)$
24	3007	2881		17.7	$\nu_{\text{sym}}(\text{CH}_2)(\text{R}2)(75) + \nu(\text{CH})(\text{R}2)(20)$
25	3001	2875	2765	30.1	$\nu_{\text{sym}}(\text{C28H}_2)(80) + \nu_{\text{asym}}(\text{C15H}_2)(18)$
26	1579	1552	1537	66.9	$\nu(\text{N-C})(\text{R}1)(70)$
27	1523	1497		1.1	Sciss(CH_2)($\text{R}2$)(90)
28	1510	1484	1494	10.5	$\delta_{\text{asym}1}(\text{CH}_3)(70) + \text{Sciss}(\text{CH}_2)(\text{butyl})(20)$
29	1506	1480		6.9	Sciss(CH_2)(butyl)(50) + $\delta_{\text{asym}1}(\text{CH}_3)(22) + \text{Sciss}(\text{CH}_2)(\text{R}2)(20)$
30	1503	1477		6.0	Sciss(CH_2)($\text{R}2$)(35) + $\delta_{\text{asym}1}(\text{CH}_3)(30) + \text{Sciss}(\text{CH}_2)(\text{butyl})(17)$
31	1499	1474	1451	48.0	Sciss(CH_2)($\text{R}2$)(65)
32	1497	1472		113.9	Sciss(CH_2)($\text{R}2$)(60) + $\nu(\text{N-C})(\text{R}1)(15) + \beta(\text{HNC/N})(15)$
33	1495	1470		84.3	Sciss(CH_2)($\text{R}2$)(65)
34	1492	1467		1.8	Sciss(CH_2)(butyl)(40) + Sciss(CH_2)($\text{R}2$)(35) + $\delta_{\text{asym}1}(\text{CH}_3)(17)$
35	1491	1466		51.5	Sciss(CH_2)(butyl)(60) + $\delta_{\text{asym}2}(\text{CH}_3)(12)$
36	1484	1459		8.3	Sciss(CH_2)($\text{R}2$)(74) + Sciss(CH_2)(butyl)(17)
37	1483	1458		6.2	Sciss(CH_2)($\text{R}2$)(86) + Sciss(CH_2)(butyl)(10)
38	1478	1453		40.4	Sciss(CH_2)(butyl)(55) + Sciss(CH_2)($\text{R}2$)(29)
39	1420	1396	1396	4.1	$\delta_{\text{sym}}(\text{CH}_3)(85)$ (umbrella mode)
40	1417	1393		13.1	Twist(CH_2)(butyl)(50) + $\nu(\text{N-C})(\text{R}1)(15)$
41	1399	1375		1.2	Rock ₂ (CH)($\text{R}2$)(28) + Rock(CH_2)($\text{R}2$)(23) + Wag(CH_2)($\text{R}2$)(20) + $\nu(\text{CC})(\text{R}2)(12)$
42	1397	1373		1.4	Rock ₂ (CH)($\text{R}2$)(30) + Rock(CH_2)($\text{R}2$)(25) + Wag(CH_2)($\text{R}2$)(20) + $\nu(\text{CC})(\text{R}2)(12)$
43	1393	1369		0.6	Rock(CH_2)($\text{R}2$)(44) + Rock1(CH)($\text{R}2$)(29) + $\nu(\text{CC})(\text{R}2)(10)$
44	1392	1368	1368	24.8	Twist(CH_2)(butyl)(35) + $\nu(\text{N-C})(\text{R}1)(18)$
45	1379	1356		1.2	Rock(CH_2)($\text{R}2$)(52) + Rock1(CH)($\text{R}2$)(29)
46	1378	1355	1359	10.4	Twist(CH_2)(butyl)(60) + Wag(CH_2)(butyl)(15)
47	1377	1354		1.4	Rock(CH_2)($\text{R}2$)(60) + Rock1(CH)($\text{R}2$)(20)
48	1357	1334	1344	26.9	Wag(CH_2)(butyl)(45) + $\nu(\text{N-C})(\text{R}1)(40)$
49	1354	1331		1.7	Twist(CH_2)(butyl)(47) + Wag(CH_2)(butyl)(26)
50	1353	1330		0.9	Rock(CH_2)($\text{R}2$)(55) + Rock2(CH)($\text{R}2$)(40)
51	1348	1325		3.8	Rock(CH_2)($\text{R}2$)(45) + Rock1(CH)($\text{R}2$)(31) + $\nu(\text{CC})(\text{R}2)(10)$
52	1344	1321		1.6	Rock(CH_2)($\text{R}2$)(43) + Rock1(CH)($\text{R}2$)(31) + $\nu(\text{CC})(\text{R}2)(10)$
53	1340	1317	1314	8.3	Rock ₁ (CH)($\text{R}2$)(31) + $\nu(\text{CC})(\text{R}2)(18) + \text{Rock}(\text{CH}_2)(\text{R}2)(12)$
54	1315	1293	1292	7.8	Wag(CH_2)($\text{R}2$)(45) + Rock(CH_2)($\text{R}2$)(24) + $\nu(\text{CC})(\text{R}2)(10)$
55	1313	1291		5.2	Wag(CH_2)($\text{R}2$)(40) + Rock(CH_2)($\text{R}2$)(24) + $\nu(\text{CC})(\text{R}2)(18)$
56	1311	1289		26.1	Wag(CH_2)($\text{R}2$)(36) + Rock(CH_2)($\text{R}2$)(24) + $\nu(\text{CC})(\text{R}2)(18)$
57	1309	1287		42.8	Wag(CH_2)($\text{R}2$)(26) + Wag(CH_2)(butyl)(20) + Rock(CH_2)($\text{R}2$)(11) + $\nu(\text{CC})(\text{R}2)(11)$
58	1294	1272	1262	9.9	Wag(CH_2)(butyl)(45) + Twist(CH_2)(butyl)(30)

Table 5. continued

s. no.	theoretical (cm ⁻¹)		exp. (cm ⁻¹)	IR int.	PED {relative phases and % contribution (more than 5%)}
	unsc.	sc.			
59	1284	1262		0.6	Wag(CH ₂)(R2)(40) + Rock ₂ (CH) (R2)(23) + ν (CC)(R2)(15)
60	1281	1259		0.5	Wag(CH ₂)(R2)(45) + Rock ₂ (CH) (R2)(25) + ν (CC)(R2)(11)
61	1255	1234		15.6	ν (N-C)(R1)(46) + β (HNC/N)(45)
62	1247	1226	1225	72.9	Wag(CH ₂)(butyl)(38) + ν (N-C)(R1)(27) + ν (N2-C7)(11)
63	1210	1189		2.5	Rock1(CH)(R2)(30) + Wag(CH ₂)(R2)(28) + β (CCC)(R2)(20)
64	1207	1186		0.7	Rock1(CH)(R2)(35) + Wag(CH ₂)(R2)(30) + β (CCC)(R2)(24)
65	1198	1178	1190	40.3	ν (N-C)(R1)(18) + Rock(CH ₂)(butyl)(15) + δ 2(R1)(15) + ν (C-S)(11)
66	1165	1145	1183,1136	32.4	Rock(CH ₂)(butyl)(30) + δ 2(R1)(18) + ν (C-S)(11)
67	1141	1122		0.1	Wag(CH ₂)(R2)(60) + Rock2(CH) (R2)(25) + Rock(CH ₂)(R2)(17)
68	1135	1116		0.0	Wag(CH ₂)(R2)(52) + Rock2(CH) (R2)(30) + Rock(CH ₂)(R2)(20)
69	1127	1108	1103	5.3	ν (N-N)(R1)(17) + Twist(CH ₂)(R2)(15) + Rock ₁ (CH)(R2)(13) + Rock(CH ₂)(R2)(10)
70	1125	1106		2.7	ν (CC _{butyl})(20) + Rock1(CH ₃)(15) + Rock(CH ₂)(butyl)(14) + Sciss(CCC/N)(butyl)(12)
71	1121	1102		2.7	Twist(CH ₂)(R2)(44) + Rock2(R2)(CH)(24) + δ (R2)(15) + β (CCC)(R2)(13)
72	1121	1102		1.9	Twist(CH ₂)(R2)(44) + Rock1(R2)(CH)(24) + δ (R2)(15) + β (CCC)(R2)(13)
73	1111	1092	1091	42.8	ν (N-N) (R1)(50) + Twist(CH ₂)(R2)(10)
74	1072	1054		0.5	ν (CC _{butyl})(81)
75	1068	1050	1052	11.8	δ (R2)(50) + β (CCC)(R2)(21) + ν (N-C)(R1)(12)
76	1049	1031		0.0	ν (CC)(R2)(55) + ν (N-C)(R1)(32)
77	1047	1029		0.5	ν (CC)(R2)(52) + ν (N-C)(R1)(20)
78	1043	1025		0.0	ν (CC)(R2)(75)
79	1000	983	992	4.2	δ (R2)(20) + ν (N-C)(R1)(15) + Wag(CH ₂)(butyl)(12)
80	983	966	975	1.1	ν (CC _{butyl})(30) + Twist(CH ₂)(R2)(20) + ν (CC)(R2)(17)
81	982	965	970	1.3	ν (CC _{butyl})(30) + Twist(CH ₂)(R2)(22) + ν (CC)(R2)(17)
82	981	964		0.7	ν (CC _{butyl})(32) + Rock1(CH ₃)(24) + ν (CC)(R2)(20)
83	976	959		1.3	ν (CC _{butyl})(28) + ν (CC)(R2)(20)
84	944	928	939	6.4	ν (CC)(R2)(55)
85	940	924		0.3	ν (CC)(R2)(65)
86	937	921	893	7.9	Rock(CH ₂)(butyl)(25) + ν (N-C)(R1)(14) + ν (CC)(R2)(13)
87	895	880	883	0.0	Twist(CH ₂)(R2)(82) + ν (CC)(R2)(15)
88	893	878		0.0	Twist(CH ₂)(R2)(80) + ν (CC)(R2)(18)
89	889	874		0.0	Twist(CH ₂)(R2)(82) + ν (CC)(R2)(15)
90	881	866	850	0.4	ν (CC _{butyl})(64) + Sciss(CCC/N)(butyl)(15)
91	854	839	815	0.6	ν (CC)(R2)(40) + δ (R2)(21) + ν (C6-C11)(13)
92	819	805		0.6	ν (CC)(R2)(60) + δ (R2)(14)
93	814	800		1.7	ν (CC)(R2)(66) + δ (R2)(17)
94	788	775	779	6.6	Rock(CH ₂)(butyl)(50) + Rock2(CH3)(23)
95	775	762	741	4.9	ν (CC)(R2)(35) + Rock(CH ₂)(butyl)(22)
96	764	751	725	6.0	ν (CC)(R2)(40) (RBM) + Rock(CH ₂)(butyl)(24)
97	732	720	719	7.3	Rock(CH ₂)(butyl)(20) + Y(HNNC/CCNN)(17) + Y(CNCC)(12) + τ 2(R1)(10)
98	724	712		4.0	τ 1(R1)(28) + Y(HNNC/CCNN)(20) + Rock(CH ₂)(butyl)(17)
99	686	674	682	1.6	ν (CC)(R2)(30) + Sciss(CH ₂)(R2)(20) + τ 2(R1)(10)
100	683	671	666	9.7	τ 2(R1)(70) + Y(SCNN)(10)
101	656	645	645	0.1	δ (R2)(50) + β (CCC)(R2)(21) + ν (CC)(R2)(12) + Twist(CH ₂)(R2)(10)
102	653	642	618	0.0	δ (R2)(47) + β (CCC)(R2)(20) + ν (CC)(R2)(12) + Twist(CH ₂)(R2)(10)
103	588	578	580	9.3	ν (C-S)(25) + β (CNC)(15) + δ 2(R1)(10)
104	530	521	507	67.1	Y(HNNC/CCNN)(64) + τ 1(R1)(20)
105	507	498	466	3.3	β (CCN)(30) + β (SCN)(15) + β (CNC)(11)
106	464	456	461	1.5	δ (R2)(40) + Twist(CH ₂)(R2)(19)
107	457	449	436	1.0	δ (R2)(40) + τ 1(R1)(20) + Twist(CH ₂)(R2)(12)
108	441	434	431	0.1	δ (R2)(65) + Twist(CH ₂)(R2)(20)
109	437	430	421	2.0	Sciss(CCC/N)(butyl)(40) + δ (R2)(15)
110	421	414	417	0.2	δ (R2)(30) + τ 1(R1)(17) + Sciss(CCC/N)(butyl)(15) + β (CCC)(R2)(10)
111	408	401	409	0.3	δ (R2)(60) + β (CCC)(R2)(20)
112	401	394	403	0.2	δ (R2)(35) + τ 1(R1)(17)
113	364	358		1.1	δ (R2)(40) + Sciss(CCC/N)(butyl)(30)
114	341	335		2.6	Y(CNCC)(25) + Sciss(CCC/N)(butyl)(25) + δ (R2)(17)
115	318	313		0.0	δ (R2)(75)
116	306	301		0.2	τ 1(R1)(40) + δ (R2)(36) + Y(HNNC/CCNN)(15)
117	300	295		0.7	Sciss(CCC/N)(butyl)(30) + τ (N2-C7)(15)

Table 5. continued

s. no.	theoretical (cm ⁻¹)		exp. (cm ⁻¹)	IR int.	PED {relative phases and % contribution (more than 5%)}
	unsc.	sc.			
			FTIR		
118	274	269		3.0	$\tau(\text{N2-C7})(25) + \beta(\text{CNC})(23)$
119	253	249		1.3	$\tau(\text{C28-C39})(25) + \beta(\text{SCN})(20) + \nu(\text{C6-C11})(15)$
120	236	232		1.3	$\delta(\text{R2})(25) + \tau(\text{C28-C39})(15) + \nu(\text{C6-C11})(15)$
121	198	195		0.5	$\tau(\text{C28-C39})(35) + \text{Sciss}(\text{CCC/N})(\text{butyl})(25)$
122	175	172		0.4	$\tau_2(\text{R1})(65) + \Upsilon(\text{HNNC/CCNN})(15)$
123	135	133		0.2	$\tau(\text{N2-C7})(45) + \tau(\text{C15-C28})(20) + \tau(\text{C28-C39})(10)$
124	110	108		0.3	$\tau(\text{C6-C11})(40) + \tau(\text{N2-C7})(35)$
125	102	100		0.2	$\tau(\text{C6-C11})(30) + \tau(\text{N2-C7})(15)$
126	77	76		0.2	$\tau(\text{N2-C7})(35) + \tau(\text{C15-C28})(25) + \tau(\text{C6-C11})(20)$
127	57	56		0.8	$\tau(\text{C6-C11})(40) + \tau_2(\text{R1})(18) + \Upsilon(\text{HNNC/CCNN})(15)$
128	34	33		0.2	$\tau(\text{C7-C15})(45) + \tau(\text{N2-C7})(16) + \tau(\text{C15-C28})(11)$
129	26	26		0.3	$\tau(\text{N2-C7})(40) + \Upsilon(\text{HNNC/CCNN})(15) + \Upsilon(\text{CNCC})(15) + \text{Rock2}(\text{R2})(\text{CH})(10)$

^aAbbreviations: ν —stretching, sym—symmetric, asy—asymmetric, δ —deformation, δ_{trig} —trigonal, β —in-plane bending, γ —out-of-plane bending, wag—wagging, rock—rocking, τ —torsion, τ_1 and τ_2 —ring torsion, twist—twisting, sciss—scissoring.

directly scaling the estimated wavenumbers with an appropriate scaling factor. All of these methods work well in addressing the issue. An empirical uniform scaling factor of 0.983 up to 1700 cm⁻¹ and that of 0.958 for larger than 1700 cm⁻¹ have been used in this study to offset the aforesaid errors. Utilizing the MOLVIB software (version V7.0-G77) designed by Sundius,³⁷ we performed a comprehensive normal coordinate analysis to project the percentage distribution of potential energy (PED) among the normal vibrational modes of the molecule under investigation. The relative intensities, line shape, and potential energy distribution (PED) were used as the key factors for the complete vibrational spectrum assignments that were carried out. Table 5 contains a tabulation of the observed and calculated scaled vibrational wavenumbers as well as the anticipated infrared intensities and full vibrational assignments, together with their percentage potential contributions. A visual comparison of the observed FT-IR and simulated spectra (Figure 6) shows a good coherence between the two spectra. The simulated and observed FT-IR spectra of 5A4BT at the DFT/B3LYP level using the 6-311+G(d, p) basis set are shown in Figure 6 for the purpose of providing a visual comparison. As 5A4BT consists of a 1,2,4-triazole ring with a substituted S atom, an adamantyl cage, and a butyl group, its vibrational modes are analyzed under three separate groups: (i) thione-substituted 1,2,4-triazole ring vibrations; (ii) adamantane cage vibrations; and (iii) butyl group vibrations.

3.4.1. Thione-Substituted 1,2,4-Triazole Ring Vibrations.

The vibrational spectrum of the sulfur-substituted 1,2,4-triazole ring contains signatures of stretching vibrations like N–N, C–N, C=N, C–S, and N–H. Additionally, N–H and C–S (in-plane and out-of-plane) bending vibrations, as well as torsional vibrations and ring deformation, are also reflected in the spectrum. The C–N stretching vibrations have a higher tendency to mix with other vibrational modes, making it difficult to perceive and assign in the spectrum. According to the findings of Al-Tamimi and colleagues,⁵⁷ the distinctive C=N absorption band of the 1,2,4-triazole ring was reported to occur at 1556 cm⁻¹. In the present case, the predominant C=N stretching mode of the sulfur-substituted 1,2,4-triazole moiety is theoretically assigned at 1552 cm⁻¹. This is a good match with the band observed at 1537 cm⁻¹ in the FT-IR spectrum. The ring N–N stretching vibration was ascribed to the band at 1091 cm⁻¹ in the experimental FT-IR spectrum of

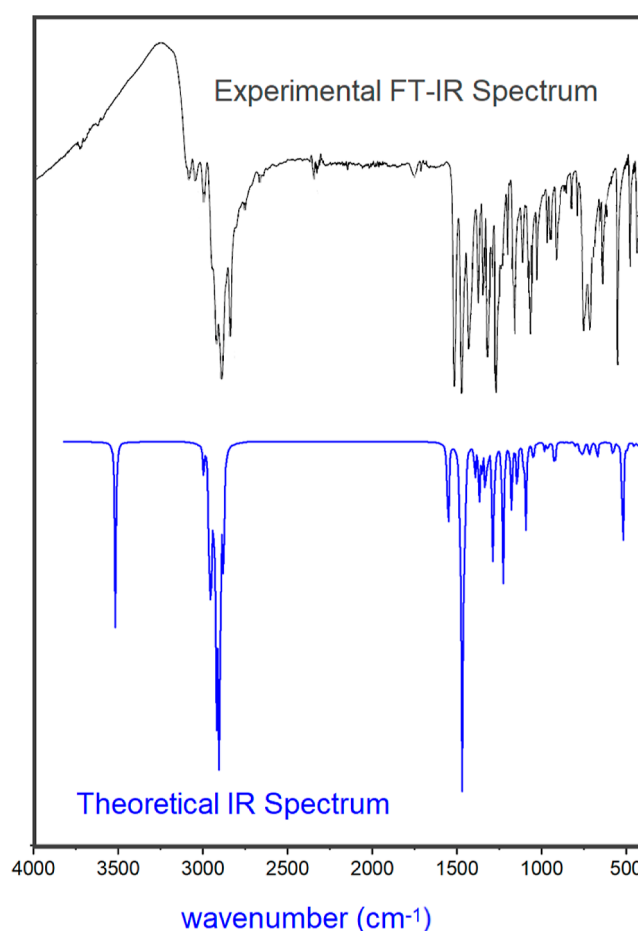


Figure 6. Experimental and theoretical IR spectra of 5A4BT.

the title compound. This band is also in excellent agreement with the scaled wavenumber, which was calculated to be at 1092 cm⁻¹. In the FT-IR spectrum, the absorption band that was seen at 580 cm⁻¹ has been identified as the main C–S stretching mode. This band also has a strong connection with the corresponding theoretical scaled wavenumber of 578 cm⁻¹.

3.4.2. Adamantane Cage Vibrations. With 10 carbon atoms in a cage skeleton in sp³-hybridized state, the adamantyl group is made up of three coalesced cyclohexane rings stacked in an “armchair” configuration with six CH₂ and three CH

groups attached to it. The adamantyl group mainly shows the stretching of C–H and C–C bonds, C–C–C angle deformation, C–C–H bending, and C–C–C–C torsional vibrations along with the vibrational modes of the CH₂ group. Each CH₂ group shows symmetric and antisymmetric stretching vibrations and in-plane and out-of-plane bending vibrations like rocking, scissoring, wagging, and twisting. Compared with symmetric stretching vibrations, the antisymmetric stretching vibrations of the CH₂ group in the adamantane cage appear at higher frequencies. Here, the computed scaled vibrational wavenumbers for the antisymmetric stretching vibrations of the CH₂ group are found at 2954, 2953, 2935, 2922, 2916, and 2915 cm⁻¹, while the C–H stretching mode containing the symmetric vibrations of the CH₂ group have been calculated at wavenumbers 2919, 2909, 2894, 2884, 2883, and 2881 cm⁻¹. The observed bands at 2930 and 2901 cm⁻¹ in the FT-IR spectrum of 5A4BT have been allocated to CH₂ antisymmetric stretching vibrations; on the other hand, the CH₂ symmetric stretching mode has been attributed to the moderately intense band at 2850 cm⁻¹. The simulated vibrational data of the title molecule show three prominent C–H stretching vibrations of the adamantane moiety, occurring at wavenumbers 2905, 2902, and 2896 cm⁻¹. The CH₂ scissoring vibrations of the adamantane ring is in general found to occur in the range 1500–1440 cm⁻¹.⁵⁸ For 5A4BT, the CH₂ scissoring mode is calculated at 1477, 1474, 1472, 1470, 1459, and 1458 cm⁻¹. The CH₂ wagging modes appear in the range of 1293–1116 cm⁻¹. Table 5 illustrates a closer alignment between the experimental spectroscopic results and the theoretical assignments, indicating a strong correspondence between them. The band at 725 cm⁻¹ in the experimental FT-IR spectrum of the title compound is identified as the symmetrical C–C stretching (cage breathing) mode of the adamantane cage which is in consonance with the calculated scaled wavenumber at 751 cm⁻¹ and also in good agreement with the reported assigned wavenumbers for the same mode in the literature at 729,⁵⁹ 742,⁵⁷ and 720 cm⁻¹.⁶⁰

3.4.3. *n*-Butyl Group Vibrations. The vibrational modes associated with the butyl group are basically C–C stretching, CH₂-symmetric, asymmetric stretching, scissoring, wagging, and twisting vibrations along with the primary vibrations such as asymmetric/symmetric C–H stretching, deformation, and torsional modes of H–C–H and C–C–H angle-bending vibrations of the CH₃ group. The band corresponding to the asymmetric stretching vibration of the bridge CH₂ moiety of the butyl group appeared at 3092 cm⁻¹ in the FT-IR spectrum of 5A4BT, while the same mode for other two CH₂ moieties was assigned at lower wavenumbers 2948 and 2918 cm⁻¹. The simulated symmetric CH₂ stretching vibrations were found at lower wavenumbers (2944, 2906, and 2875 cm⁻¹) in comparison to the corresponding asymmetric modes. The calculated wavenumbers 2964 and 2959 cm⁻¹ with more than 90% contribution to PED were assigned to asymmetrical stretching of the CH₃ group, and the calculated wavenumber at 2901 cm⁻¹ was assigned to the CH₃ symmetric stretching mode with 95% PED. The dominant asymmetrical/symmetrical (Umbrella mode) deformations of the CH₃ group have been identified with a medium intensity band at 1494/1396 cm⁻¹ in the FT-IR region and are in complete coherence with the corresponding simulated wavenumbers at 1484 and 1396 cm⁻¹, respectively.

3.5. FMO, MESP, and Reactivity Descriptors (Global and Local). FMOs, specifically HOMO and LUMO, are vital

for comprehending the reactivity of molecules. By the analysis of the energy values and characteristics of these orbitals, one can make predictions about reaction mechanisms, selectivity, and the overall chemistry of molecules. The visuals of HOMO and LUMO along with the other significant MOs for 5A4BT are presented in Figure 7.

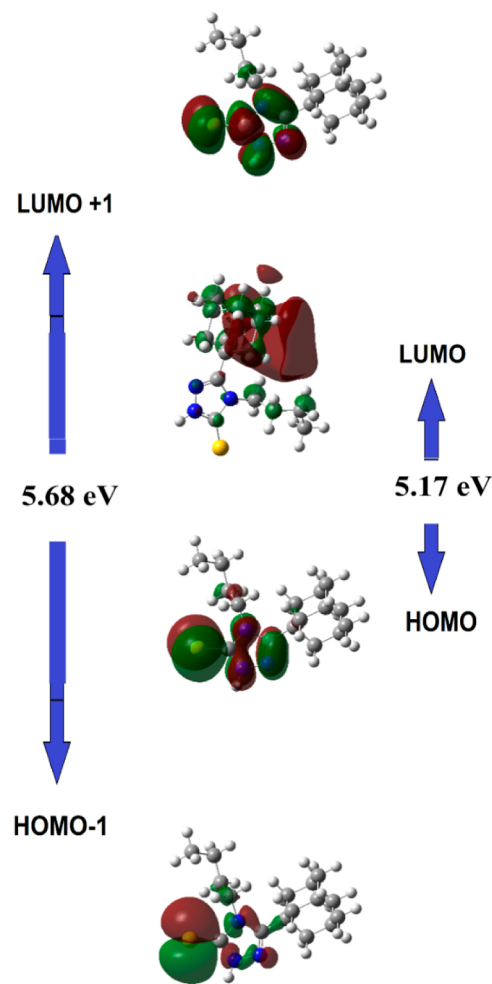


Figure 7. HOMO, LUMO, and other prominent molecular orbitals of 5A4BT.

The molecular electrostatic potential map (MESP) is a sophisticated computational chemistry tool that offers an insightful glance into the intricate electrostatic potential distribution within a molecule. As the electron density within a molecule influences electrostatic forces among the atoms, understanding the MESP landscape becomes very important in deducing the molecule's chemical behavior and reactivity. By analyzing the MESP, one can determine which region of a molecule is electrophilic (electron-poor) or nucleophilic (electron-rich). MESP may be used to predict the binding affinity of a small molecule to a protein's active site in the context of drug design and molecular docking investigations. Regions exhibiting analogous electrostatic potentials often favor strong intermolecular interactions, a key phenomenon in understanding biological processes. Figure 8 depicts the MESP plot of 5A4BT.

DFT descriptors are important parameters to understand the molecular properties, interactions, and reactivities of drug candidates. These descriptors provide insights into stability,

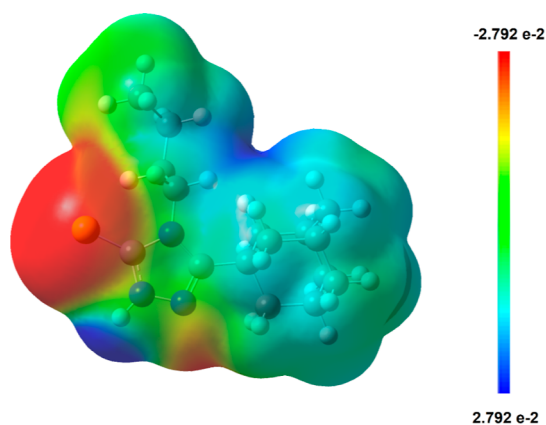


Figure 8. MESP plot of 5A4BT.

electronic structure, and charge distribution,^{46,47} hence aiding rational drug designing. DFT was used to estimate quantum chemical descriptors such as the ionization potential, electronegativity, electron affinity, chemical potential, hardness, softness, and electrophilicity index of 5A4BT. Using the difference between the ground-state energies of the cationic and neutral systems, as well as the neutral and anionic systems, respectively, the ionization potential of the molecule is estimated to be 7.51223 eV, and the electron affinity of the molecule is calculated to be -0.47891 eV. Using the Parr and Pearson theory,^{61–63} the electronic chemical potential (IP + EA)/2 may be used to compute the electron escaping tendency from a stable system. Electronegativity (χ) is the negative of the electronic chemical potential (μ). Chemical hardness expressed as $\eta = (\text{IP} - \text{EA})/2$ indicates resistance to electron distribution changes and correlates with stability and reactivity. The global softness given as $S = (1/\eta)$ is the inverse of the hardness. Parr and Yang,⁶⁴ created the global electrophilicity index $\omega = \mu^2/2\eta$, which measures energy loss from the maximum electron flow between the donor and acceptor using chemical potential and hardness. The chemical hardness for the title molecule is 3.99557 eV. Table 6 shows the global reactivity descriptor values for 5A4BT.

Table 6. Calculated Global Reactivity Descriptors for 5A4BT at the B3LYP/6-311+G(d, p) Level

ionization potential	(IP) (eV)	7.51223
electron affinity	(EA) (eV)	-0.47891
electronegativity	(χ) (eV)	3.51666
chemical potential	(μ) (eV)	-3.51666
chemical hardness	(η) (eV)	3.99557
global softness	(S) (eV^{-1})	0.25028
global electrophilicity index	(ω) (eV)	1.54758

When the number of electrons in a particular chemical species (molecule) is altered, the local reactivity descriptor, such as the Fukui function, demonstrates the most favorable regions in which the density of the chemical species will change. Alternatively, it specifies the predisposition of the electronic density to deform at a specific location when electrons are accepted or donated.^{64,65} The condensed or atomic Fukui functions on the k th atomic position for electrophilic (f_k^-), nucleophilic (f_k^+), and free-radical (f_k^0) attacks can be calculated as $f_k^+ = [q(N+1)] - q(N)$; $f_k^- = [q(N) - q(N-1)]$; and $f_k^0 = 1/2[q(N+1) - q(N-1)]$,

respectively. Here, q_k represents the atomic charge at the k th atomic position in the anionic (charge = +1), cationic (charge = -1), or neutral molecule (charge = 0). It has been demonstrated by Parr and Yang^{64,65} that the sites in chemical species that have the highest values of the Fukui function (f_k) have a significant degree of reactivity for the corresponding attacks. It has been established that the Fukui functions derived from the NBO charges are well accepted.⁶⁶ For 5A4BT, the values of computed Fukui functions using NBO charges given in Table 7 and graphically shown in Figure 9 indicate that in the 5A4BT compound the preferred reactive atomic sites for nucleophilic attacks are in the order C28 > C36 > C31 > C21 > C26 > C12 > C33 > S1 > C24 > C43 >

Table 7. Values of the Fukui Functions Based on NBO Charges

atoms	f_k^+	f_k^-	f_k^0
S1	0.0442	0.5358	0.2900
N2	-0.0094	0.0824	0.0365
N3	0.0092	0.1003	0.0548
N4	0.0066	0.0961	0.0513
H5	0.0094	0.0285	0.0190
C6	-0.0054	0.0687	0.0317
C7	0.0256	-0.0111	0.0073
H8	-0.0070	0.0288	0.0109
H9	0.0088	0.0011	0.0049
C10	0.0004	-0.0697	-0.0347
C11	0.0080	-0.0086	-0.0003
C12	0.0694	0.0018	0.0356
H13	0.0112	0.0049	0.0081
H14	0.0068	-0.0027	0.0020
C15	0.0229	0.0076	0.0152
H16	0.0123	-0.0161	-0.0019
H17	0.0001	0.0144	0.0073
C18	0.0339	-0.0029	0.0155
H19	0.0114	0.0000	0.0057
H20	0.0101	0.0020	0.0061
C21	0.0738	0.0030	0.0384
H22	0.0052	-0.0008	0.0022
H23	0.0128	0.0037	0.0083
C24	0.0399	-0.0007	0.0196
H25	0.0169	0.0153	0.0161
C26	0.0736	-0.0005	0.0366
H27	0.0158	0.0160	0.0159
C28	0.0949	-0.0061	0.0444
H29	0.0011	0.0138	0.0074
H30	0.0124	0.0185	0.0154
C31	0.0865	-0.0008	0.0428
H32	0.0149	0.0148	0.0149
C33	0.0472	-0.0029	0.0222
H34	0.0126	0.0051	0.0089
H35	0.0115	0.0148	0.0132
C36	0.0885	-0.0026	0.0430
H37	0.0150	0.0153	0.0151
H38	0.0081	0.0019	0.0050
C39	0.0115	-0.0032	0.0042
H40	0.0123	0.0218	0.0171
H41	0.0103	-0.0022	0.0041
H42	0.0028	-0.0027	0.0000
C43	0.0392	-0.0029	0.0182
H44	0.0110	0.0150	0.0130
H45	0.0137	0.0049	0.0093

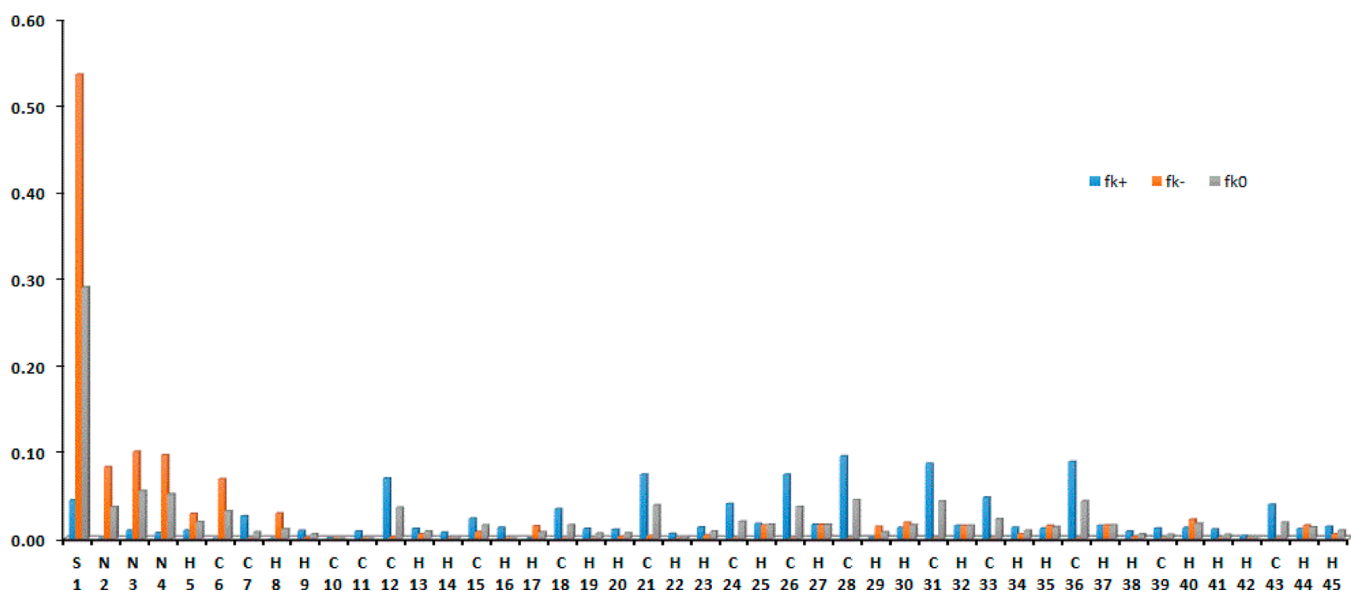


Figure 9. Fukui function for 5A4BT.

C18 > C7 > C15, and the preferred atomic sites for electrophilic reactivity are in the order S1 > N3 > N4 > N2 > C6 > H8 > H5 > H40 > H30, while the reactivity order of sites for f_k^0 is S1 > N3 > N4 > C28 > C36 > C31 > C21 > C26 > N2 > C12 > C6 > C33 > C24.

3.6. Molecular Docking. Inflammation is central to many chronic diseases and is frequently associated with pain. Inflammation is caused by prostaglandins, which are targeted by nonsteroidal anti-inflammatory medications (NSAIDs). COX is a crucial enzyme that converts arachidonic acids into prostaglandins. COX-1 is consistently expressed and associated with the initiation of inflammatory responses, whereas COX-2 is implicated in inflammation and breast cancer. COX-1 is overexpressed in the malignancies of the epidermis, breast, colorectum, and ovary.⁶⁷

The title compound, 5A4BT, was docked into the binding sites of COX-1 with PDB entry 3KK6 in complex with celecoxib⁶⁸ and COX-2 using the PDB entry 1CX2 cocrystallized with SC-558.⁶⁹ The target proteins in PDB format were taken from the RCSB protein data bank. UCSF Chimera⁷⁰ was utilized to scrap cocrystallized ligands along with all the chains other than chain A and was saved as a PDB file. These PDB files of target proteins and the PDB file of the title compound were converted into PDBQT files which, respectively, act as input target proteins and ligand in the process of docking in Auto Dock Vina software.⁴³ Figure 10a,b depicts the target proteins 3KK6 and 1CX2. Polar hydrogen atoms were incorporated into the protein structures prior to the docking

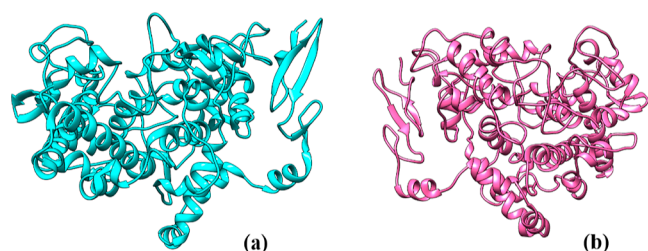


Figure 10. Target proteins (a) COX-1 (PDB 3KK6) and (b) COX-2 (PDB 1CX2).

process. The sizes of the grid for 3KK6 and 1CX2 were set to $19 \times 30 \times 26$ and $25 \times 28 \times 25$, respectively. The grid center coordinates (x, y, z) for 3KK6 and 1CX2 were determined to be $-28.515, 38.505, -7.533$ and $22.312, 16.170, 17.740$, respectively.

The literature indicates that the three structural domains found in each monomer of COX are the membrane-binding domain, the catalytic domain, and the epidermal growth factor domain. The catalytic domain is where substrate binding and NSAID activity take place. Both COX-1 and COX-2 contain a hydrophobic channel that runs from the membrane-binding domain to the center of the catalytic domain. This channel is narrowed by three residues, namely Tyr-355, Arg-120, and Glu-524, and these three residues separate the channel into the lobby region and the substrate-/inhibitor-binding site of COX.⁷¹ The residues in the lobby region that are found to be significant for inhibitor interactions are reported to be Pro-86, Ile-89, Leu-93, and Val-116.⁷¹ To analyze the interactions between the target proteins and the ligand, Discovery Studio Visualizer⁷² was used in the present study. It reveals a hydrogen-bonding interaction between the 5A4BT and Glu-524 residues in the 3KK6 protein as well as van der Waals interactions involving the Leu357, Tyr355, His90, and Pro86 residues. The 5A4BT and 3KK6 carbon–hydrogen bond involves the residue Val 116. In the docked structures of 5A4BT and 3KK6, all residues crucial for inhibitor interactions, such as with Pro86, Ile-89, Leu-93, and Val-116,⁷¹ are present. The van der Waals interactions between 5A4BT and 1CX2 involve the amino acid residues Arg120, Val116, Ile92, and Lys83, which are crucial for inhibitory interactions. 5A4BT displayed binding affinities of -6.4 and -6.5 kcal/mol, respectively, for the target proteins PDB 3KK6 and 1CX2. The 2D and 3D interactions of the docked structure are shown, respectively, in Figure 11a,b for 5A4BT-3KK6 and Figure 11c,d for 5A4BT-1CX2.

3.7. ADME Properties, Drug Likeness, and Toxicity. The utilization of in silico ADME prediction has become an indispensable instrument in enhancing the process of selecting the most promising drug candidates for subsequent development. During the drug discovery phase, emphasis has been

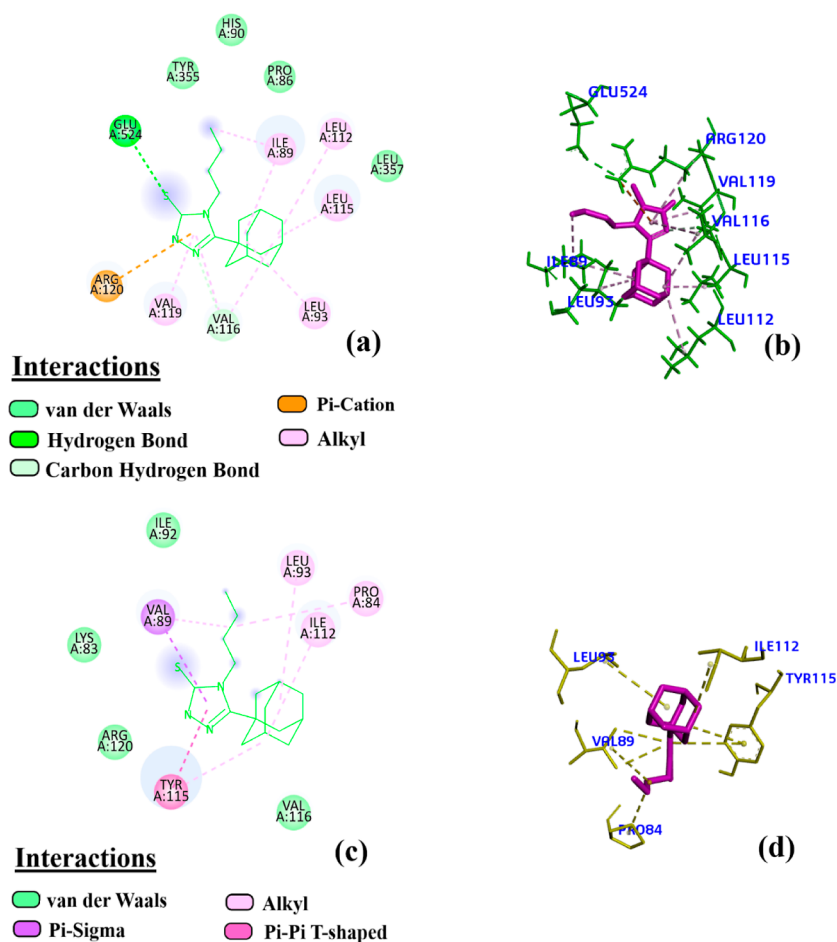


Figure 11. Interactions between target proteins (PDB: 3KK6) and the ligand 5A4BT in (a) 2D view and (b) 3D view and interactions between target proteins (PDB: 1CX2) and the ligand 5A4BT in (c) 2D view and (d) 3D view.

placed on the early detection of unfavorable absorption, distribution, metabolism, and excretion (ADME) characteristics to eliminate drug candidates with poor ADME characteristics.

Using the online tool SwissADME,⁷³ Protox-II,⁷⁴ and ADMETlab 2.0⁷⁵ pharmacokinetics, drug-likeness, bioavailability, and toxicity were computationally predicted. Oral drugs have to cross intestinal cell membranes via passive diffusion, carrier-mediated absorption, or active transport before entering the systemic circulation. Due to their physical and functional similarities, the human colon adenocarcinoma cell lines (Caco-2) are often utilized to estimate *in vivo* drug permeability instead of the intestinal epithelium. The Caco-2 cell permeability index is also relevant for the proposed drug candidates. A compound with anticipated Caco-2 permeability $> -5.15 \log \text{ cm/s}$ is expected to be a suitable drug molecule. The predicted Caco-2 cell permeability of 5A4BT is $-4.613 \log \text{ cm/s}$. Madin–Darby Canine Kidney (MDCK) cells are an *in vitro* permeability screening model. The *in vitro* gold standard for chemical absorption efficiency is its apparent permeability coefficient, P_{app} . P_{app} values of MDCK cell lines are used to measure the BBB impact. The title compound with $P_{app} = 2.6 \times 10^{-5} > 2 \times 10^{-6} \text{ cm/s}$, shows strong MDCK permeability.

A compound is supposed to have a valid plasma protein binding (PPB) if its projected value is $<90\%$. Volume distribution is crucial for drug *in vivo* distribution. Based on

its VD value, we may estimate an unknown compound's PPB, bodily fluid distribution, and tissue absorption. A compound has a correct VD if its expected VD is 0.04–20 L/kg. The title compound shows decent values for PPB (81.94) and VD (1.217). NSAIDs block the activity of cyclooxygenases (COX) with different COX1/COX2 inhibition profiles, and it has been proved that NSAIDs can cross the BBB both in humans as well as in several animals. The title compound is estimated to be BBB-permeant. The bioavailability score is evaluated to be 0.55, and a high GI absorption is predicted. As far as pharmacokinetic filters are concerned, 5A4BT satisfies the following rules: the Veber rule,⁷⁶ the Ghose rule,⁷⁷ the Muegge rule,⁷⁸ and the Egan rule.⁷⁹ A molecule's drug-likeness is known to depend on these rules/filters. Compounds satisfying the golden triangle rule⁸⁰ are expected to have more favorable properties as compared to those that do not go along with the rule. The golden triangle rule was designed by combining *in vitro* permeability, clearance, and computer modeling to assist medicinal chemists in uncovering physiologically stable, permeable, and effective drug candidates. The title compound satisfies the golden triangle rule as well. The pharmacokinetics, ADMET, and drug-likeness properties are collected in Table 8.

3.8. Molecular Dynamics Simulation. For the ability to analyze the time-dependent behavior of any molecular system, especially conformational alterations during protein–ligand interactions, and for detailed microscopic modeling at the

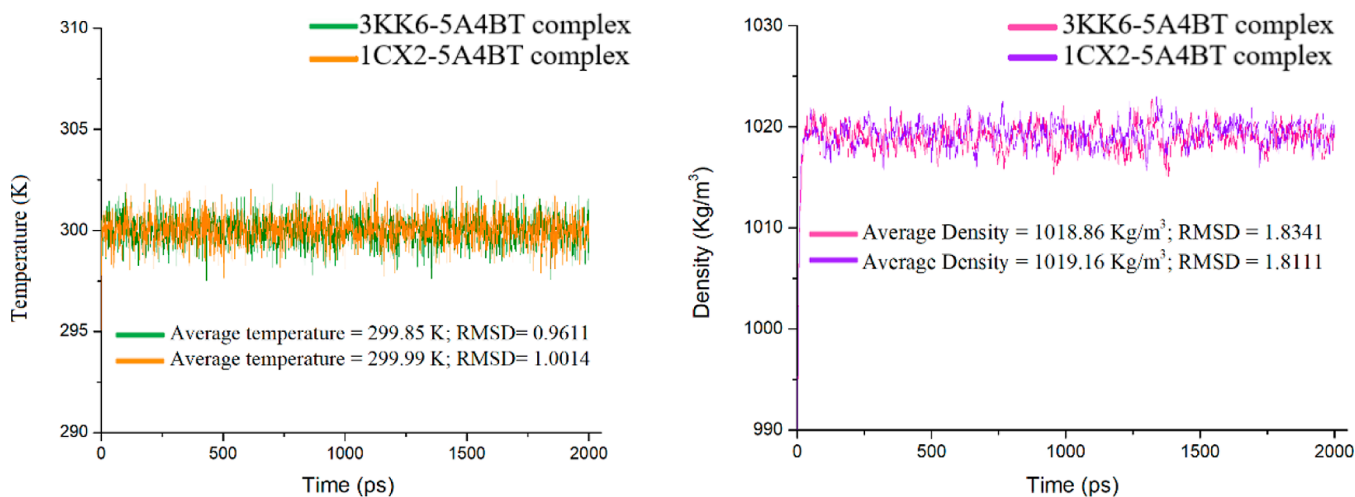
Table 8. Pharmacokinetics, ADMET, and Drug-Likeness Properties of 5A4BT

properties	values/properties/activity
molecular weight (g/mol)	291.45
topological polar surface area Å ²	65.70
number of hydrogen-bond acceptors	3
number of hydrogen-bond donors	1
number of rotatable bonds	4
molecular refractivity	84.86
octanol/water partition coefficient (log <i>P</i>)	4.079
BBB permeant	yes
Lipinski	yes
Veber	yes
Muegge	yes
Egan	yes
golden triangle rule	satisfied
bioavailability score	0.55
Toxicity	
dili	inactive
carcinogenicity	inactive
immunotoxicity	inactive
mutagenicity	inactive
cytotoxicity	inactive
aryl hydrocarbon receptor (AhR)	inactive
androgen receptor (AR)	inactive
androgen receptor ligand-binding domain (AR-LBD)	inactive
aromatase	inactive
estrogen receptor alpha (ER)	inactive
estrogen receptor ligand-binding domain (ER-LBD)	inactive
peroxisome proliferator-activated receptor gamma (PPAR-Gamma)	inactive
nuclear factor (erythroid-derived 2)-like 2/antioxidant-responsive element (nrf2/ARE)	inactive
heat shock factor response element (HSE)	inactive
mitochondrial membrane potential (MMP)	inactive
phosphoprotein (tumor suppressor) p53	inactive
ATPase family AAA domain-containing protein 5 (ATAD5)	inactive

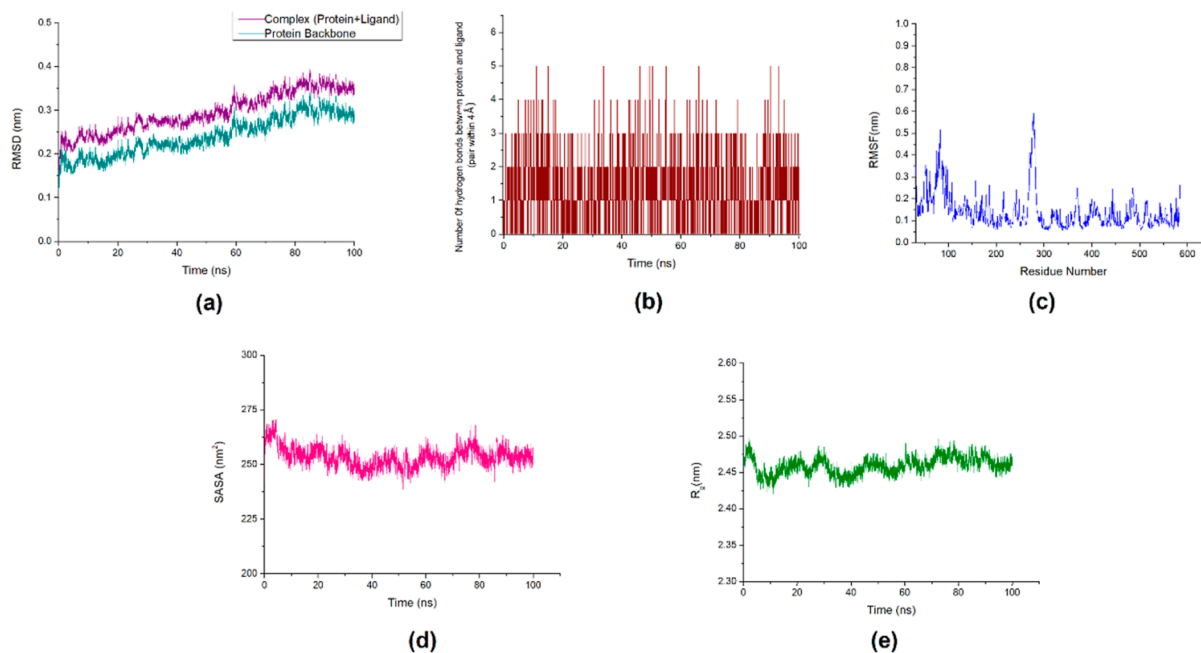
molecular scale, MD simulation methods have become invaluable in both pure and applied research.

Proteins are considered rigid in fixed molecular docking; therefore, MD simulations are required to account for the conformational changes that occur during ligand–protein docking. The GROMACS software (2021.1 version)^{44–48} was used to conduct MD simulations on the docked complexes of 3KK6 and 1CX2 with 5A4BT. The topology file for the proteins was prepared which contains all the information about the molecules like atomic masses, bond lengths, bond angles, and charges. Charmm force field with the three-point (TIP3P) water model was selected for topology calculation. After that, the topology file of ligand was created using the CgenFF server (<https://cgenff.umaryland.edu>) and then included into the topology parameters for the proteins separately. Lastly, a “position restraint file” is formed, which is used for *NVT/NPT* equilibration. Target proteins and the ligand complex were put in a cubic dodecahedron simulation box and filled with water molecules. The spc216.gro model, a generic equilibrated three-point explicit water model,⁸¹ was used for solvation, and no ions were added to the 3KK6–5A4BT system since the system was already electrically neutral, and three sodium ions were added to make the 1CX2–5A4BT complex electrically neutral. To stop thermodynamically unfavorable interactions, the steepest descent energy minimization method was used.⁴⁷ Subsequently, the systems were equilibrated in two steps—*NVT* ensemble for 2000 ps and *NPT* ensemble for 10,000 ps (10 ns), both at a temperature of 300 K.⁸² In the *NPT* ensemble, the pressure was maintained at 1 bar. During the *NVT* equilibration, the solvent is allowed to move freely around the protein while the protein is held fixed in place. This is done by using a position-restraint file that was previously generated. Specifying this restraint, the protein movement is not totally forbidden but is energetically penalized. During the *NPT* step, the restraints were removed.

In order to regulate the temperature at 300 K, a modified Berendsen thermostat⁸³ was implemented. This thermostat is more efficient and ergodic than the Nose–Hoover thermostat, and it also addresses the limitations of the original Berendsen thermostat. The pressure was maintained at 1 bar using a Parrinello–Rahman barostat⁸² with a time constant of 2 ps and an isotropic compressibility of 4.5×10^{-5} bar. The average temperature for the 3KK6–5A4BT complex and the 1CX2–5A4BT complex was determined to be 299.85 and 299.99 K, respectively, after *NVT* equilibration, while the root-mean-

**Figure 12.** Variation of the density and temperature after *NVT* and *NPT* equilibration.

(A) 3KK6-5A4BT Complex



(B) 1CX2-5A4BT Complex

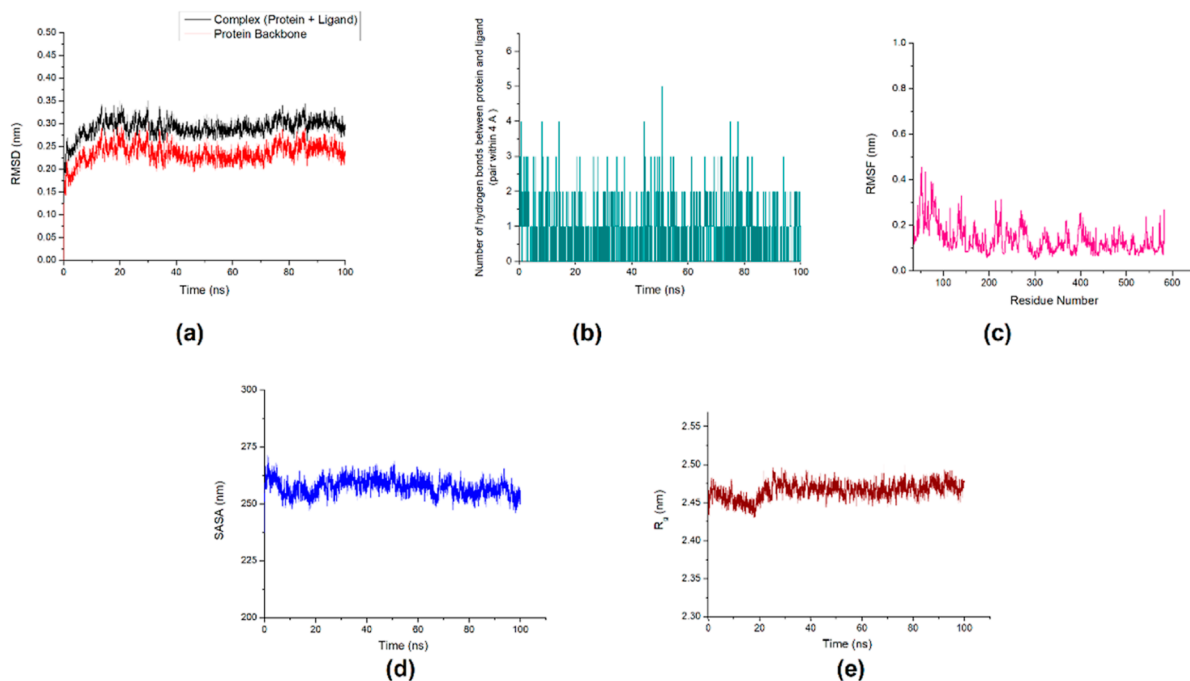


Figure 13. Profile of MD simulation for (A) 3KK6–5A4BT complex and (B) 1CX2–5A4BT complex. (a) rmsd for the protein and protein–ligand complex, (b) number of hydrogen bonds during 100 ns MD simulation of the complex, (c) RMSF values for individual residues, (d) SASA of the complex, and (e) radius of gyration of the complex.

square deviation (rmsd) for the two complexes was 0.9611 and 1.0014 (error estimates of 0.012 and 0.021), and the average density was found to be 1018.86 and 1019.16 kg/m³ following *NPT* equilibration, with an rmsd of 1.8341 and 1.8111 (error estimates of 0.086 and 0.15). Figure 12 shows a time plot of the temperature and density variations.

The modified Berendsen thermostat was used with a barostat to keep the system's pressure at 1.01325 bar and

temperature at 300 K during MD simulation after the equilibration (*NVT* and *NPT*) process is complete. During a 100 ns MD simulation, the atom coordinates of the system were saved every 10 ps. Utilizing VMD⁸⁴ and UCSF Chimera,⁷⁰ images and trajectory data have been produced.

To examine the MD trajectory equilibration, the protein and complex are computed for rmsd. rmsd measures how much a ligand, protein, or ligand–protein complex departs from the

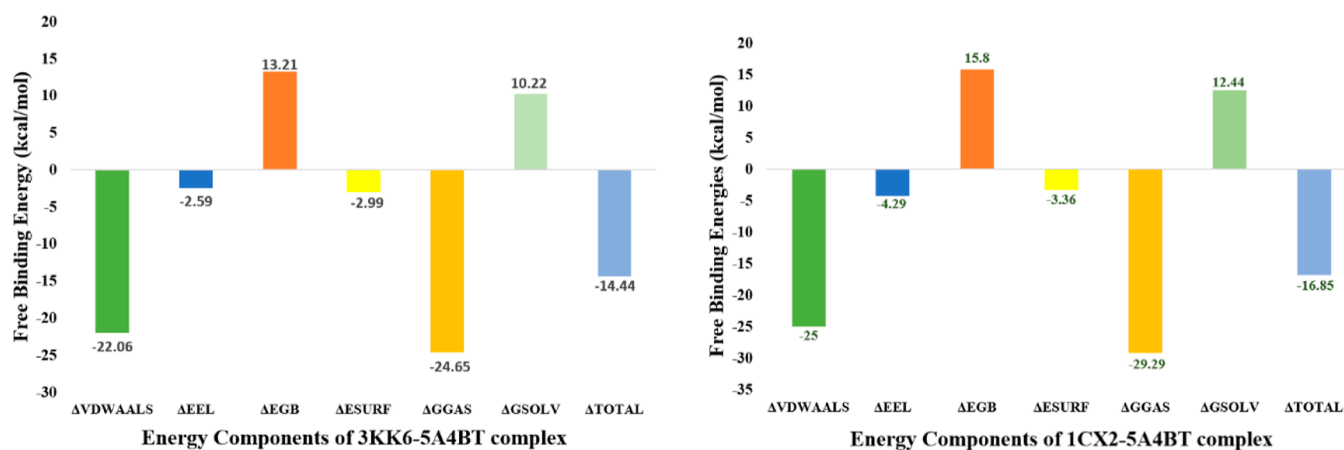


Figure 14. Various energy components of the 3KK6–5A4BT and 1CX2–5A4BT complexes.

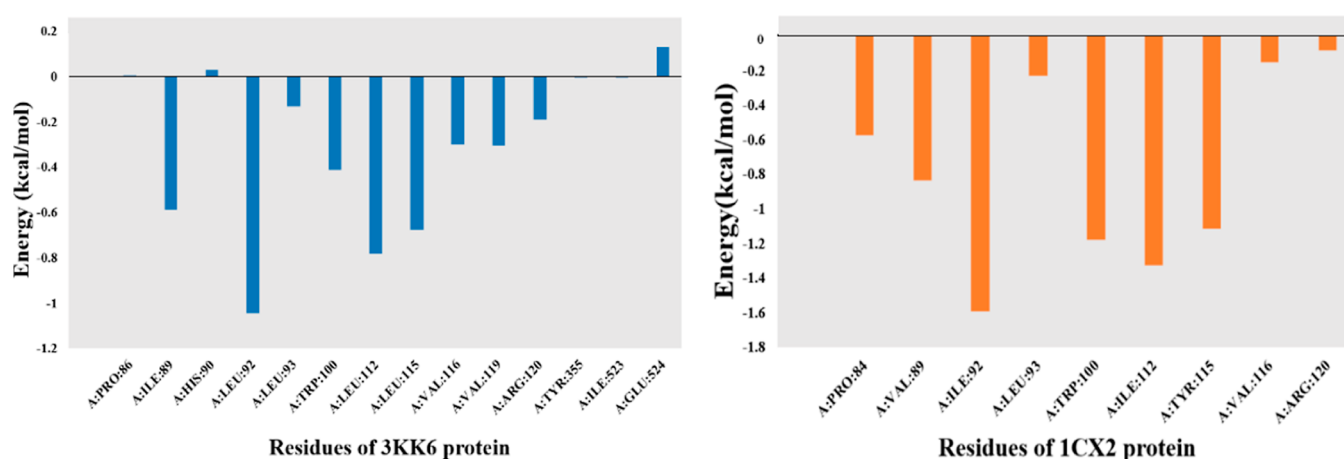


Figure 15. Molecular mechanics-generalized Born surface area (MMGBSA) energy decomposition of residues of the protein in 3KK6–5A4BT and 1CX2–5A4BT complexes.

reference structure. The analysis reveals low RMSD values and the complex's structural stability. The rmsd profile for the 1CX2–5A4BT complex becomes almost constant after 25 ns. Figure 13a shows the rmsd graphs for proteins and ligand–protein complexes.

Figure 13b–e provides plots of hydrogen bonding between ligand and residues of binding cavity, RMSF, SASA, and R_g , respectively. Root-mean-square fluctuation measures a protein residue's mean deviation from a reference position over a period of time. The maximum or minimum deviation of the various residues from their mean structure is represented by RMSF. The RMSF profile shows that the binding site of 3KK6 fluctuates below 0.25 nm [Figure 13A(c)], whereas the total variation is between 0.05 and 0.50 nm, whereas for COX-2, the RMSF values remains well below 0.4 nm [Figure 13B(c)] except for the terminal residues. The radius of gyration measures the protein compactness. It shows how regular secondary structures fill the three-dimensional structure of a protein. The “gmx gyrate” command analyzed R_g throughout the MD trajectory. The radius of gyration fluctuated up to 25 and 20 ns, respectively, for the two complexes, but the simulation run ended in a stable conformation. The SASA plot for the 3KK6–5A4BT complex fluctuated for 25 ns before stabilizing until the simulation was completed, whereas the SASA plot for the 1CX2–5A4BT complex remains almost constant throughout the simulation. During 100 ns MD

simulations, the hydrogen-bond plots for the two complexes revealed an average of three or two hydrogen bonds between the ligand and residues of the binding pocket. The MD simulation results suggest that the dynamic stability of the 1CX2–5A4BT complex is more as compared to the 3KK6–5A4BT complex.

3.9. MMGBSA Analysis. The MM-GBSA approach is an efficient and reliable binding free energy simulation method to assert the affinity of the ligand for its receptor. The approach is based on MD simulations of the receptor–ligand complex.²⁵ The binding free energies of the 3KK6–5A4BT and 1CX2–5A4BT complexes were determined using this approach. Figure 14 shows the various energy components of the 3KK6–5A4BT and 1CX2–5A4BT complexes. For both complexes, the contribution of the van der Waals interaction (Δ VDWAALS) to the binding energy dominates over the contribution of the electrostatic interaction (Δ EEL). The contributions of van der Waals interaction and electrostatic interaction are greater for the COX-2 (1CX2)–5A4BT complex as compared to the COX-1 (3KK6)–5A4BT complex. The obtained total binding energies for 3KK6–5A4BT and 1CX2–5A4BT complexes are -14.44 and -16.85 kcal/mol, respectively, which indicate the greater binding affinity of 5A4BT toward the COX-2 (1CX2) receptor than the COX-1 (3KK6) receptor. Using the decomposition analysis of MMGBSA, the contributions of amino acid residues

of 3KK6 and 1CX2 proteins in their respective complexes with 5A4BT were calculated. The residues and the corresponding energies for both complexes are shown in Figure 15. The residues crucial for the COX inhibitor interactions, i.e., PRO-86, ILE-89, LEU-93, and VAL-116, show significant contributions in both receptor–ligand complexes.

4. CONCLUSIONS

In this study, we investigated the structural and pharmacological properties of 5-(adamantan-1-yl)-4-butyl-2,4-dihydro-3H-1,2,4-triazole-3-thione (5A4BT), a hybrid compound incorporating both the adamantyl moiety and the triazolone-thiol group. The work aimed at identifying the therapeutic use of this compound, as a potential COX inhibitor, by combining theoretical and experimental methodologies. The X-ray crystal analysis revealed strong intermolecular hydrogen bonding, as well as other weaker interactions like $\pi\cdots\pi$ and C–H $\cdots\pi$ interactions, which collectively contribute to the compound's supramolecular structure. The IR spectrum also revealed an extensive network of interactions present in the system. Molecular docking studies with COX-1 (3KK6) and COX-2 (1CX2) proteins with binding affinities of -6.4 and -6.5 kcal/mol, respectively, and interactions with crucial residues within the protein-binding sites demonstrated the potential of 5A4BT as a COX inhibitor.

Replicating physiological conditions, the MD simulations provided further confirmation of the stability and dynamic behavior of ligand–protein complexes within a water-filled environment for a 100 ns duration. By employing MM-GBSA analysis, the total binding energies of the complexes 3KK6–5A4BT and 1CX2–5A4BT were determined to be -14.44 and -16.85 kcal/mol, respectively, reflecting that 5A4BT exhibits a significantly greater affinity for binding to the COX-2 receptor in comparison to the COX-1 receptor. Furthermore, the assessment of ADME properties revealed promising pharmacokinetic profiles, drug-likeness, and low toxicity, suggesting the compound's suitability for further drug development. The study lays foundational groundwork for potential therapeutic uses of 5-(adamantan-1-yl)-4-butyl-2,4-dihydro-3H-1,2,4-triazole-3-thione as a COX inhibitor in treating inflammatory conditions and managing pain; however, further *in vivo* investigations are vital to validate these findings.

5. EXPERIMENTAL SECTION

The investigated compound 5A4BT was synthesized via the reaction of adamantane-1-carbohydrazide with butyl isothiocyanate to yield the corresponding thiosemicarbazides, followed by cyclization by heating in 10% aqueous sodium hydroxide solution as previously reported.¹⁴ The pure single crystals of 5A4BT were acquired by a gradual evaporation of its 1:1 v/v solution in ethanol/chloroform held at room temperature. Crystallographic data are deposited on CCDC under deposition number 2334265. CIF file can be accessed at no cost through the access structure applet in the CCDC webpage (<https://www.ccdc.cam.ac.uk/structures>).

AUTHOR INFORMATION

Corresponding Authors

Ali A. El-Emam – Department of Medicinal Chemistry, Faculty of Pharmacy, Mansoura University, Mansoura 35516, Egypt; orcid.org/0000-0002-9325-9497; Email: elemam@mans.edu.eg

Leena Sinha – Department of Physics, University of Lucknow, Lucknow 226007 Uttar Pradesh, India; orcid.org/0000-0003-3624-4085; Email: sinhaleena27@gmail.com

Authors

Lamya H. Al-Wahaibi – Department of Chemistry, College of Sciences, Princess Nourah bint Abdulrahman University, Riyadh 11671, Saudi Arabia

Mohammed S. M. Abdelbaky – Department of Physical and Analytical Chemistry, Faculty of Chemistry, Oviedo University-CINN, Oviedo 33006, Spain; orcid.org/0000-0001-8395-8705

Santiago Garcia-Granda – Department of Physical and Analytical Chemistry, Faculty of Chemistry, Oviedo University-CINN, Oviedo 33006, Spain; orcid.org/0000-0002-2373-0247

Anushree Maurya – Department of Physics, University of Lucknow, Lucknow 226007 Uttar Pradesh, India

Mamta Pal – Department of Physics, University of Lucknow, Lucknow 226007 Uttar Pradesh, India

Zohra Siddiqui – Department of Physics, University of Lucknow, Lucknow 226007 Uttar Pradesh, India

Raj Shukla – Department of Physics, University of Lucknow, Lucknow 226007 Uttar Pradesh, India

Shilendra K. Pathak – Department of Physics, M. M. M. P. G. College, Deoria 274502 Uttar Pradesh, India

Ruchi Srivastava – Department of Physics, University of Lucknow, Lucknow 226007 Uttar Pradesh, India

Vikas K. Shukla – Department of Physics, Maharishi University of Information Technology, Lucknow 226013 Uttar Pradesh, India

Onkar Prasad – Department of Physics, University of Lucknow, Lucknow 226007 Uttar Pradesh, India

Complete contact information is available at:

<https://pubs.acs.org/10.1021/acsomega.4c03512>

Notes

The authors declare no competing financial interest.

ACKNOWLEDGMENTS

This research was funded by Princess Nourah bint Abdulrahman University Researchers Supporting Project no. (PNURSP2024R3), Princess Nourah bint Abdulrahman University, Riyadh, Saudi Arabia. One of the authors (R.S.) is grateful to CSIR, New Delhi, India for the research fellowship.

REFERENCES

- (1) Wanka, L.; Iqbal, K.; Schreiner, P. R. The Lipophilic Bullet Hits the Targets: Medicinal Chemistry of Adamantane Derivatives. *Chem. Rev.* **2013**, *113* (5), 3516–3604.
- (2) Davies, W. L.; Grunert, R. R.; Haff, R. F.; McGahan, J. W.; Neumeyer, E. M.; Paulshock, M.; Watts, J. C.; Wood, T. R.; Hermann, E. C.; Hoffmann, C. E. Antiviral activity of 1-adamantamine (amantadine). *Science* **1964**, *114*, 862–863.
- (3) Wendel, H. A.; Snyder, M. T.; Pell, S. Trial of amantadine in epidemic influenza. *Clin. Pharmacol. Ther.* **1966**, *7*, 38–43.
- (4) Wingfield, W. L.; Pollack, D.; Grunert, R. R. Therapeutic Efficacy of Amantadine HCl and Rimantadine HCl in Naturally Occurring Influenza A2 Respiratory Illness in Man. *N. Engl. J. Med.* **1969**, *281*, 579–584.
- (5) Rosenthal, K. S.; Sokol, M. S.; Ingram, R. L.; Subramanian, R.; Fort, R. C. Tromantadine: Inhibitor of early and late events in herpes

- simplex virus replication. *Antimicrob. Agents Chemother.* **1982**, *22*, 1031–1036.
- (6) Arshad, N.; Saeed, A.; Perveen, F.; Ujan, R.; Farooqi, S. I.; Ali Channar, P.; Shabir, G.; El-Seedi, H. R.; Javed, A.; Yamin, M.; Bolte, M.; Hökelek, T. Synthesis, X-ray, Hirshfeld surface analysis, exploration of DNA binding, urease enzyme inhibition and anticancer activities of novel adamantane-naphthyl thiourea conjugate. *Bioorg. Chem.* **2021**, *109*, 104707.
- (7) Lorenzo, P.; Alvarez, R.; Ortiz, M. A.; Alvarez, S.; Piedrafita, F. J.; de Lera, A. R. Inhibition of I κ B Kinase- β and Anticancer Activities of Novel Chalcone Adamantyl Arotinoids. *J. Med. Chem.* **2008**, *51*, 5431–5440.
- (8) Han, T.; Goralski, M.; Capota, E.; Padrick, S. B.; Kim, J.; Xie, Y.; Nijhawan, D. The antitumor toxin CD437 is a direct inhibitor of DNA polymerase α . *Nat. Chem. Biol.* **2016**, *12*, 511–515.
- (9) Dai, L.; Smith, C. D.; Foroozesh, M.; Miele, L.; Qin, Z. The sphingosine kinase 2 inhibitor ABC294640 displays anti-non-small cell lung cancer activities in vitro and in vivo. *Int. J. Cancer* **2018**, *142*, 2153–2162.
- (10) Hassan, H. M.; Al-Wahaibi, L. H.; Shehatou, G. S.; El-Emam, A. A. Adamantane-linked isothiourea derivatives suppress the growth of experimental hepatocellular carcinoma via inhibition of TLR4-MyD88-NF- κ B signaling. *Am. J. Cancer Res.* **2021**, *11* (2), 350–369.
- (11) Zoidis, G.; Fytas, C.; Papanastasiou, I.; Foscolos, G. B.; Fytas, G.; Padalko, E.; De Clercq, E.; Naesens, L.; Neyts, J.; Kolocouris, N. Heterocyclic rimantadine analogues with antiviral activity. *Bioorg. Med. Chem.* **2006**, *14*, 3341–3348.
- (12) Pérez-Pérez, M. J.; Balzarini, J.; Hosoya, M.; De Clercq, E.; Camarasa, M. J. Synthesis of adamantane-spirosulfones as potential antiviral agents. *Bioorg. Med. Chem. Lett.* **1992**, *2*, 647–648.
- (13) Van Derpoorten, K.; Balzarini, J.; De Clercq, E.; Poupaert, J. H. Anti-HIV activity of N-1-adamantyl-4-aminophthalimide. *Biomed Pharmacother.* **1997**, *51*, 464–468.
- (14) El-Emam, A. A.; Ibrahim, T. M. Synthesis, anti-inflammatory and analgesic activity of certain 3-(1-adamantyl)-4-substituted-5-mercapto-1,2,4-triazole derivatives. *Arzneimittel-forschung* **1991**, *41*, 1260–1264.
- (15) Al-Omar, M. A.; Al-Abdullah, E. S.; Shehata, I. A.; Habib, E. E.; Ibrahim, T. M.; El-Emam, A. A. Synthesis, antimicrobial, and anti-inflammatory activities of novel 5-(1-adamantyl)-4-arylideneamino-3-mercapto-1,2,4-triazoles and related derivatives. *Molecules* **2010**, *15*, 2526–2550.
- (16) Kadi, A. A.; El-Brollosy, N. R.; Al-Deeb, O. A.; Habib, E. E.; Ibrahim, T. M.; El-Emam, A. A. Synthesis, antimicrobial, and anti-inflammatory activities of novel 2-(1-adamantyl)-5-substituted-1,3,4-oxadiazoles and 2-(1-adamantylamino)-5-substituted-1,3,4-thiadiazoles. *Eur. J. Med. Chem.* **2007**, *42*, 235–242.
- (17) Kouatly, O.; Geronikaki, A.; Kamoutsis, C.; Hadjipavlou-Litina, D.; Eleftheriou, P. Adamantane derivatives of thiazolyl-N-substituted amide, as possible non-steroidal anti-inflammatory agents. *Eur. J. Med. Chem.* **2009**, *44*, 1198–1204.
- (18) Baxter, A.; Bent, J.; Bowers, K.; Braddock, M.; Brough, S.; Fagura, M.; Lawson, M.; McNally, T.; Mortimore, M.; Robertson, M.; et al. Hit-to-Lead studies: The discovery of potent adamantane amide P2X7 receptor antagonists. *Bioorg. Med. Chem. Lett.* **2003**, *13*, 4047–4050.
- (19) Fresno, N.; Pérez-Fernández, R.; Goicoechea, C.; Alkorta, I.; Fernandez-Carvajal, A.; de la Torre-Martínez, R.; Quirce, S.; Ferrer-Montiel, A.; Martín, M. I.; Goya, P.; et al. Adamantyl Analogues of Paracetamol Potent Analgesic Drugs via Inhibition of TRPA1. *PLoS One* **2014**, *9* (12), No. e113841.
- (20) Tozkoparan, B.; Küpeli, E.; Yeşilada, E.; Ertan, M. Preparation of 5-aryl-3-alkylthio-1,2,4-triazoles and corresponding sulfones with anti-inflammatory-analgesic activity. *Bioorg. Med. Chem.* **2007**, *15*, 1808–1814.
- (21) Navidpour, L.; Shafaroodi, H.; Abdi, K.; Amini, M.; Ghahremani, M. H.; Dehpour, A. R.; Shafiee, A. Design, synthesis, and biological evaluation of substituted 3-alkylthio-4,5-dialkyl-4H-1,2,4-triazoles as selective COX-2 inhibitors. *Bioorg. Med. Chem.* **2006**, *14*, 2507–2517.
- (22) Abdelrazeq, A. S.; Ghabbour, H. A.; Al-Wahaibi, L. H.; Abdelbaky, M. S. M.; Garcia-Granda, S.; El-Emam, A. A.; Pathak, S. K.; Srivastava, R.; Maurya, A.; Shukla, V. K.; Prasad, O.; Sinha, L. Synthesis, Spectroscopic Analysis, Molecular Docking, Molecular Dynamics Simulation of 5-(Adamantan-1-yl)-4-(3-Chlorophenyl)-2,4-Dihydro-3H-1,2,4-Triazole-3-Thione, a Potential Anti-proliferative Agent. *Polycycl. Aromat. Comp.* **2023**, *44*, 2553.
- (23) Šermukšnytė, A.; Kantminienė, K.; Jonuškienė, I.; Tumosienė, I.; Petrikaitė, V. The Effect of 1,2,4-Triazole-3-thiol Derivatives Bearing Hydrazone Moiety on Cancer Cell Migration and Growth of Melanoma, Breast, and Pancreatic Cancer Spheroids. *Pharmaceuticals* **2022**, *15* (8), 1026.
- (24) Timur, I.; Kocyigit, Ü. M.; Dastan, T.; Sandal, S.; Ceribasi, A. O.; Taslimi, P.; Gulcin, İ.; Koparir, M.; Karatepe, M.; Çiftçi, M. in vitro cytotoxic and in vivo antitumoral activities of some aminomethyl derivatives of 2,4-dihydro-3H-1,2,4-triazole-3-thiones—Evaluation of their acetylcholinesterase and carbonic anhydrase enzymes inhibition profiles. *J. Biochem. Mol. Toxicol.* **2019**, *33*, No. e22239.
- (25) Bader, R. F. W. A quantum theory of molecular structure and its applications. *Chem. Rev.* **1991**, *91* (5), 893–928.
- (26) Genheden, S.; Ryde, U. The MM/PBSA and MM/GBSA methods to estimate ligand-binding affinities. *Expert Opin. Drug Discovery* **2015**, *10*, 449–461.
- (27) Kohn, W.; Sham, L. J. Self-Consistent Equations Including Exchange and Correlation Effects. *Phys. Rev.* **1965**, *140*, A1133–A1138.
- (28) Becke, A. D. Density-functional thermochemistry. III. The role of exact exchange. *J. Chem. Phys.* **1993**, *98*, 5648–5652.
- (29) Lee, C.; Yang, W.; Parr, R. G. Development of the Colle-Salvetti Correlation-energy Formula into a Functional of the Electron Density. *Phys. Rev. B: Condens. Matter* **1988**, *37* (2), 785.
- (30) Miehlich, B.; Savin, A.; Stoll, H.; Preuss, H. Results Obtained with the Correlation Energy Density Functionals of Becke and Lee, Yang and Parr. *Chem. Phys. Lett.* **1989**, *157*, 200–206.
- (31) Frisch, M. J.; Trucks, G. W.; Schlegel, H. B.; Scuseria, G. E.; Robb, M. A.; Cheeseman, J. R.; Scalmani, G.; Barone, V.; Petersson, G. A.; Nakatsuji, H.; et al. *Gaussian 09*, Revision D.01; Gaussian, Inc: Wallingford, CT, 2009.
- (32) Frisch, E.; Hratchian, H. P.; Dennington, R. D.; Keith, T. A.; Millam, J.; Nielsen, B.; Holder, A. J.; Hiscococks, J. *GaussView (Version 5.0.8)*; Gaussian, Inc: Wallington, 2009.
- (33) Singh, I.; Al-Wahaibi, L. H.; Srivastava, R.; Prasad, O.; Pathak, S. K.; Kumar, S.; Parveen, S.; Banerjee, M.; El-Emam, A. A.; Sinha, L. DFT Study on the Electronic Properties, Spectroscopic Profile, and Biological Activity of 2-Amino-5-trifluoromethyl-1,3,4-thiadiazole with Anticancer Properties. *ACS Omega* **2020**, *5*, 30073–30087.
- (34) Foresman, J. B.; Frisch, A. *Exploring Chemistry with Electronic Structure Methods*, 2nd ed.; Gaussian Inc.: Pittsburgh PA, 1996.
- (35) Pulay, P.; Fogarasi, G.; Pang, F.; Boggs, J. E. Systematic ab initio gradient calculation of molecular geometries, force constants, and dipole moment derivatives. *J. Am. Chem. Soc.* **1979**, *101* (10), 2550–2560.
- (36) Fogarasi, G.; Zhou, X.; Taylor, P. W.; Pulay, P. The calculation of ab initio molecular geometries: efficient optimization by natural internal coordinates and empirical correction by offset forces. *J. Am. Chem. Soc.* **1992**, *114* (21), 8191–8201.
- (37) Sundius, T. A new damped least-squares method for the calculation of molecular force fields. *J. Mol. Spectrosc.* **1980**, *82* (1), 138–151.
- (38) Sundius, T. Molvib - A flexible program for force field calculations. *J. Mol. Struct.* **1990**, *218*, 321–326.
- (39) Sundius, T. Scaling of ab initio force fields by MOLVIB. *Vib. Spectrosc.* **2002**, *29* (1–2), 89–95.
- (40) Buckingham, A. D. Permanent and Induced Molecular Moments and Long-Range Intermolecular Forces. *Adv. Chem. Phys.* **1967**, *12*, 107–142.

- (41) Glendening, E. D.; Landis, C. R.; Weinhold, F. Natural bond orbital methods. *Wiley Interdiscip. Rev.: Comput. Mol. Sci.* **2012**, *2* (1), 1–42.
- (42) Johnson, E. R.; Keinan, S.; Mori-Sanchez, P.; Contreras-García, J.; Cohen, A. J.; Yang, W. Revealing Noncovalent Interactions. *J. Am. Chem. Soc.* **2010**, *132* (18), 6498–6506.
- (43) Trott, O.; Olson, A. J. AutoDock Vina: improving the speed and accuracy of docking with a new scoring function, efficient optimization, and multithreading. *J. Comput. Chem.* **2010**, *31* (2), 455–461.
- (44) Abraham, M. J.; Murtola, T.; Schulz, R.; Pall, S.; Smith, J. C.; Hess, B.; Lindahl, E. GROMACS: High Performance Molecular Simulations through Multi-level Parallelism from Laptops to Supercomputers. *SoftwareX* **2015**, *1-2*, 19–25.
- (45) Páll, S.; Abraham, M. J.; Kutzner, C.; Hess, B.; Lindahl, E. Tackling Exascale Software Challenges in Molecular Dynamics Simulations with GROMACS. *Proceedings of the Exascale Applications and Software Conference*, 2014; Vol. 8759, pp 3–27.
- (46) Pronk, S.; Pall, S.; Schulz, R.; Larsson, P.; Bjelkmar, P.; Apostolov, R.; Shirts, M. R.; Smith, J. C.; Kasson, P. M.; van der Spoel, D.; et al. GROMACS 4.5: A High-throughput and Highly Parallel Open-Source Molecular Simulation Toolkit. *Bioinformatics* **2013**, *29* (7), 845–854.
- (47) Hess, B.; Kutzner, C.; van der Spoel, D.; Lindahl, E. GROMACS 4: Algorithms for Highly Efficient, Load-balanced, and Scalable Molecular Simulation. *J. Chem. Theory Comput.* **2008**, *4* (3), 435–447.
- (48) Van Der Spoel, D.; Lindahl, E.; Hess, B.; Groenhof, G.; Mark, A. E.; Berendsen, H. J. GROMACS: Fast, Flexible, and Free. *J. Comput. Chem.* **2005**, *26* (16), 1701–1718.
- (49) Szafran, M.; Komasa, A.; Bartoszak-Adamska, E. Crystal and molecular structure of 4-carboxypiperidinium chloride (4-piperidine-carboxylic acid hydrochloride). *J. Mol. Struct.* **2007**, *827*, 101–107.
- (50) Sebastian, S.; Sundaraganesan, N. The spectroscopic (FT-IR, FT-IR gas phase, FT-Raman and UV) and NBO analysis of 4-Hydroxypiperidine by density functional method. *Spectrochim. Acta, Part A* **2010**, *75*, 941–952.
- (51) Shainyan, B. A.; Chiparina, N. N.; Aksamentova, T. N.; Oznobikhina, L. P.; Rosentsveig, G. N.; Rosentsveig, I. B. Intramolecular hydrogen bonds in the sulfonamide derivatives of oxamide, dithiooxamide, and biuret. FT-IR and DFT study, AIM and NBO analysis. *Tetrahedron* **2010**, *66*, 8551–8556.
- (52) Carroll, M. T.; Bader, R. F. W. An analysis of the hydrogen bond in BASE-HF complexes using the theory of atoms in molecules. *Mol. Phys.* **1988**, *65*, 695–722.
- (53) Koch, U.; Popelier, P. L. A. Characterization of C-H-O Hydrogen Bonds on the Basis of the Charge Density. *J. Phys. Chem.* **1995**, *99*, 9747–9754.
- (54) Espinosa, E.; Molins, E.; Lecomte, C. Hydrogen bond strengths revealed by topological analyses of experimentally observed electron densities. *Chem. Phys. Lett.* **1998**, *285*, 170–173.
- (55) Targema, M.; Obi-Egbedi, N. O.; Adeoye, M. D. Molecular structure and solvent effects on the dipole moments and polarizabilities of some aniline derivatives. *Comput. Theor. Chem.* **2013**, *1012*, 47–53.
- (56) Willow, S. Y.; Xie, B.; Lawrence, J.; Eisenberg, R. S.; Minh, D. D. L. On the polarization of ligands by proteins. *Phys. Chem. Chem. Phys.* **2020**, *22*, 12044–12057.
- (57) Al-Tamimi, A. M. S.; El-Emam, A. A.; Al-Deeb, O. A.; Prasad, O.; Pathak, S. K.; Srivastava, R.; Sinha, L. Structural and spectroscopic characterization of a novel potential anti-inflammatory agent 3-(adamantan-1-yl)-4-ethyl-1H-1,2,4-triazole-5(4H)thione by first principle calculations. *Spectrochim. Acta, Part A* **2014**, *124*, 108–123.
- (58) Bagrii, E. I. *Adamantany: Poluchenie, Svoistva, Pri-Menenie (Adamantanes: Preparation, Properties, and Application)*; Nauka: Moscow, 1989.
- (59) El-Emam, A. A.; Al-Tamimi, A. M. S.; Al-Rashood, K. A.; Misra, H. N.; Narayan, V.; Prasad, O.; Sinha, L. Structural and spectroscopic characterization of a novel potential chemotherapeutic agent 3-(1-adamantyl)-1-[[4-(2-methoxyphenyl)piperazin-1-yl]methyl]-4-methyl-1H-1,2,4-triazole-5(4H)-thione by first principle calculations. *J. Mol. Struct.* **2012**, *1022*, 49–60.
- (60) Almutairi, M. S.; Alanazi, A. M.; Al-Abdullah, E. S.; El-Emam, A. A.; Pathak, S. K.; Srivastava, R.; Prasad, O.; Sinha, L. FT-IR and FT-Raman spectroscopic signatures, vibrational assignments, NBO, NLO analysis and molecular docking study of 2-[[5-(adamantan-1-yl)-4-methyl-4H-1,2,4-triazol-3-yl]sulfanyl]-N,N-dimethylethanamine. *Spectrochim. Acta, Part A* **2015**, *140*, 1–14.
- (61) Parr, R. G.; Pearson, R. G. Absolute hardness: companion parameter to absolute electronegativity. *J. Am. Chem. Soc.* **1983**, *105*, 7512–7516.
- (62) Parr, R. G.; Chattaraj, P. K. Principle of maximum hardness. *J. Am. Chem. Soc.* **1991**, *113*, 1854–1855.
- (63) Parr, R. G.; Szentpaly, L. V.; Liu, S. J. Electrophilicity Index. *Am. Chem. Soc.* **1999**, *121*, 1922–1924.
- (64) Parr, R. G.; Yang, W. *Density-functional theory of Atoms and Molecules*; Oxford University Press: New York, Oxford, 1989.
- (65) Parr, R. G.; Yang, W. Density Functional Approach to the Frontier-Electron Theory of Chemical Reactivity. *J. Am. Chem. Soc.* **1984**, *106*, 4049–4050.
- (66) Nazari, F.; Rasoulzadeh Zali, F. Density functional study of the relative reactivity of the carbonyl group in substituted cyclohexanone. *J. Mol. Struct.: THEOCHEM* **2007**, *817*, 11–18.
- (67) Dvorakova, M.; Langhansova, L.; Temml, V.; Pavicic, A.; Vanek, T.; Landa, P. Synthesis, Inhibitory Activity, and *In Silico* Modeling of Selective COX-1 Inhibitors with a Quinazoline Core. *ACS Med. Chem. Lett.* **2021**, *12* (4), 610–616.
- (68) Rimon, G.; Sidhu, R. S.; Lauver, D. A.; Lee, J. Y.; Sharma, N. P.; Yuan, C.; Frieler, R. A.; Trievel, R. C.; Lucchesi, B. R.; Smith, W. L. Coxibs interfere with the action of aspirin by binding tightly to one monomer of cyclooxygenase-1. *Proc. Natl. Acad. Sci. U.S.A.* **2010**, *107*, 28–33.
- (69) Kurumbail, R. G.; Stevens, A. M.; Gierse, J. K.; McDonald, J. J.; Stegeman, R. A.; Pak, J. Y.; Gildehaus, D.; iyashiro, J. M.; Penning, T. D.; Seibert, K.; Isakson, P. C.; Stallings, W. C. Structural basis for selective inhibition of cyclooxygenase-2 by anti-inflammatory agents. *Nature* **1996**, *384*, 644–648.
- (70) Pettersen, E. F.; Goddard, T. D.; Huang, C. C.; Couch, G. S.; Greenblatt, D. M.; Meng, E. C.; Ferrin, T. E. UCSF Chimera - A Visualization System for Exploratory Research and Analysis. *J. Comput. Chem.* **2004**, *25*, 1605–1612.
- (71) Blobaum, A. L.; Marnett, L. J. Structural and Functional Basis of Cyclooxygenase Inhibition. *J. Med. Chem.* **2007**, *50*, 1425–1441.
- (72) Dassault Systemes Biovia. *Discovery Studio Modeling Environment*; Dassault Systemes: San Diego, 2016.
- (73) Daina, A.; Michielin, O.; Zoete, V. SwissADME: A Free Web Tool to Evaluate Pharmacokinetics, Drug-likeness and Medicinal Chemistry Friendliness of Small Molecules. *Sci. Rep.* **2017**, *7*, 42717.
- (74) Banerjee, P.; Eckert, A. O.; Schrey, A. K.; Preissner, R. ProTox-II: A Webserver for the Prediction of Toxicity of Chemicals. *Nucleic Acids Res.* **2018**, *46*, 257–263.
- (75) Xiong, G.; Wu, Z.; Yi, J.; Fu, L.; Yang, Z.; Hsieh, C.; Yin, M.; Zeng, X.; Wu, C.; Lu, A.; Chen, X.; Hou, T.; Cao, D. ADMETlab 2.0: an integrated online platform for accurate and comprehensive predictions of ADMET properties. *Nucleic Acids Res.* **2021**, *49* (W1), W5–W14.
- (76) Veber, D. F.; Johnson, S. R.; Cheng, H. Y.; Smith, B. R.; Ward, K. W.; Kopple, K. D. Molecular Properties That Influence the Oral Bioavailability of Drug Candidates. *J. Med. Chem.* **2002**, *45*, 2615–2623.
- (77) Ghose, A. K.; Viswanadhan, V. N.; Wendoloski, J. J. A Knowledge-based Approach in Designing Combinatorial or Medicinal Chemistry Libraries for Drug Discovery. 1. A Qualitative and Quantitative Characterization of Known Drug Databases. *J. Comb. Chem.* **1999**, *1*, 55–68.
- (78) Muegge, I.; Heald, S. L.; Brittelli, D. Simple Selection Criteria for Drug-like Chemical Matter. *J. Med. Chem.* **2001**, *44*, 1841.

(79) Egan, W. J.; Merz, K. M., Jr.; Baldwin, J. J. Prediction of Drug Absorption Using Multivariate Statistics. *J. Med. Chem.* **2000**, *43*, 3867–3877.

(80) Johnson, T. W.; Dress, K. R.; Edwards, M. Using the Golden Triangle to optimize clearance and oral absorption. *Bioorg. Med. Chem. Lett.* **2009**, *19* (19), 5560–5564.

(81) Berendsen, H. J. C.; Postma, J. P. M.; Gunsteren, W. F. V.; Hermans, J. Intermolecular Forces. In *Interaction Models for Water in Relation to Protein Hydration*; Pullman, B., Ed.; D. Reidel Publishing Company: Dordrecht, 1981; pp 331–342.

(82) Parrinello, M.; Rahman, A. Polymorphic transitions in single crystals: a new molecular dynamics method. *J. Appl. Phys.* **1981**, *52* (12), 7182–7190.

(83) Bussi, G.; Donadio, D.; Parrinello, M. Canonical sampling through velocity rescaling. *J. Chem. Phys.* **2007**, *126* (1), 014101.

(84) Humphrey, W.; Dalke, A.; Schulten, K. VMD: visual molecular dynamics. *J. Mol. Graph.* **1996**, *14* (1), 33–38.